③

DIAGNOSTICS DEVELOPMENT FOR E-BEAM EXCITED AIR CHANNELS

Technical Report No. 4

ELECTRICAL CONDUCTIVITY MEASUREMENTS
OF LASER-GUIDED AND EXPLODING-WIRE
DISCHARGES IN AIR

February 1989

By: K. R. Stalder, M. S. Williams, and
       D. J. Eckstrom

SRI International
333 Ravenswood Avenue
Menlo Park, CA 94025-3493
(415) 326-6200
TWX: 910-373-2046
Telex: 334486
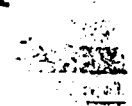
DTIC
ELECTE
S 1 7 APR 1989
E

SRI International

89

REPORT DOCUMENTATION PAGE

Form Approved
OMB No. 0704-0188

1a. REPORT SECURITY CLASSIFICATION Unclassified		1b. RESTRICTIVE MARKINGS N/A
2a. SECURITY CLASSIFICATION AUTHORITY DARPA-CG-55		3. DISTRIBUTION/AVAILABILITY OF REPORT Approved for Public Release; distribution unlimited.
2b. DECLASSIFICATION/DOWNGRADING SCHEDULE N/a		
4. PERFORMING ORGANIZATION REPORT NUMBER(S) MP 88-292		5. MONITORING ORGANIZATION REPORT NUMBER(S)
6a. NAME OF PERFORMING ORGANIZATION SRI International	6b. OFFICE SYMBOL (If applicable)	7a. NAME OF MONITORING ORGANIZATION Naval Surface Weapons Center
6c. ADDRESS (City, State, and ZIP Code) 333 Ravenswood Avenue Menlo Park, CA 94025		7b. ADDRESS (City, State, and ZIP Code) Silver Springs, MD 20910
8a. NAME OF FUNDING/SPONSORING ORGANIZATION Defense Advanced Research Agency	8b. OFFICE SYMBOL (If applicable)	9. PROCUREMENT INSTRUMENT IDENTIFICATION NUMBER Contract No. N60921-85-C-0210

8c. ADDRESS (City, State, and ZIP Code)
1400 Wilson Boulevard
Arlington, VA. 22209

10. SOURCE OF FUNDING NUMBERS

PROGRAM ELEMENT NO. 4395/54	PROJECT NO.	TASK NO.	WORK UNIT ACCESSION NO.

11. TITLE (Include Security Classification)
DIAGNOSTICS DEVELOPMENT FOR E-BEAM EXCITED AIR CHANNELS. ELECTRICAL CONDUCTIVITY MEASUREMENTS OF LASER GUIDED AND EXPLODING WIRE DISCHARGES IN AIR

12. PERSONAL AUTHOR(S)
K. R. Stalder, M.S. Williams, and D. J. Eckstrom

13a. TYPE OF REPORT Technical No. 4	13b. TIME COVERED FROM _____ TO _____	14. DATE OF REPORT (Year, Month, Day) February 1989	15. PAGE COUNT 65

16. SUPPLEMENTARY NOTATION

17. COSATI CODES			18. SUBJECT TERMS (Continue on reverse if necessary and identify by block number)
FIELD	GROUP	SUB-GROUP	Plasma Diagnostics; microwave techniques; Conductivity measurements; electron beams.

19. ABSTRACT (Continue on reverse if necessary and identify by block number)

The conductivity of reduced density channels made by laser-initiated and exploding-wire-initiated discharges was measured systematically by microwave interferometry. The results show that the DC conductivity can be as high as $5 \times 10^{10} s^{-1}$ for the laser channels and as high as $10^{11} s^{-1}$ for the exploding-wire channels. The channel temperature inferred from the conductivity levels is as high as 4000 K. The channels cool by adiabatic expansion, and subsequent turbulent convective mixing of the hot central plasma with the cold surrounding air; as a result, the conductivity drops to $5 \times 10^{9} s^{-1}$ in 2-6 ms, depending on the initial discharge energy. The effects of impurities are discussed, as are the implications for charged particle beam propagation in such channels.

20. DISTRIBUTION/AVAILABILITY OF ABSTRACT ☒ UNCLASSIFIED/UNLIMITED ☐ SAME AS RPT ☐ DTIC USERS	21. ABSTRACT SECURITY CLASSIFICATION Unclassified	
22a. NAME OF RESPONSIBLE INDIVIDUAL B. Hui	22b. TELEPHONE (Include Area Code) (202) 394-1264	22c. OFFICE SYMBOL N60921

DD Form 1473, JUN 86   Previous editions are obsolete.   SECURITY CLASSIFICATION OF THIS PAGE

CONTENTS

ILLUSTRATIONS

INTRODUCTION

Laser-guided and exploding-wire discharges have been used to create reduced-density channels for intense relativistic beam propagation studies for several years[MRP87, JFF88]. These discharges simulate the channel properties created by very high current density electron beams, where hole-boring would be the dominant mechanism for range extension. The reduced density channels may be quite hot, on the order of 4000 K, and therefore are also ionized to some extent. The degree of ionization determines the electrical conductivity of the channel, which competes with the density channel tracking mechanisms to affect the tracking stability of the electron beam in the channel. Although DC conductivity levels below 5×10^9 s^{-1} are thought to oe necessary for beam tracking, the conductivities in these simulated reduced density channels start at much higher levels and decrease to the critical level as a result of cooling by adiabatic expansion in hundreds of microseconds and subsequent turbulent convective mixing of the hot central plasma with cool air in the next few milliseconds.

The essential physics of reduced-density channels may initially be modeled by studying an ideal density channel, created by the adiabatic expansion of an azimuthally symmetric, uniformly heated, line source. An ideal density channel would have no axial or azimuthal gradients in pressure or density. If such a channel were in pressure equilibrium with the surrounding air and its temperature or density were known, its conductivity could be predicted by using Saha's equation to calculate the electron density and known momentum transfer cross sections to compute the electron collision frequency [BJS60]. An ideal channel also would cool by heat conduction, and the conductivity would decrease accordingly.

Channels created by laser-guided discharges or exploding-wire discharges, on the other hand, have strong local density and pressure gradients that drive turbulent convective mixing of the hot central plasma with the surrounding cold air. The mixing is not predictable, and consequently, neither is the conductivity. Thus, conductivity measurements are required to determine the optimum time for subsequent beam propagation.

1

In addition to the turbulence generated by such channels, the aerosols in laser-guided discharges and the metal vapors in exploding-wire discharges should be expected to greatly affect the channel's conductivity. The role of contaminants in these discharges, and their effect on the channel's electrical conductivity and cooling rate, are unknown and also necessitate direct measurements of the conductivity.

The range of conductivity levels encountered in these channels, from greater than 10^{11} s^{-1} to less than 10^9 s^{-1}, is measurable by microwave interferometric techniques. We report here measurements of the microwave conductivity in reduced density air channels created by laser-guided discharges in aerosol-seeded air and by exploding-wire-generated discharges. These measurements were obtained at the Naval Research Laboratory (NRL) charged particle beam facility. Knowing the microwave conductivity, we can compute the electron density and collision frequency or, alternatively, the DC conductivity.

It is also possible to infer the channel temperature and neutral density from the conductivity, if equilibrium air conditions are assumed, and therefore these measurements are important supplements to the neutral density measurements made with optical interferometers. Because the turbulent nature of the channels quickly washes out the optical interference fringes, the optical interferometer technique is less quantitative at late times. However, microwaves are not significantly refracted by the turbulence and therefore are useful to measure the relaxation of the density channels at late times. The assumption of equilibrium conditions for these computations allows us to compare the conductivity of the real channels to that of ideal channels and therefore to determine the effects of contaminants.

The measurements described in this report were performed on two separate occasions. The initial experiments employed a 35-GHz Mach-Zehnder interferometer to measure the conductivity of laser-guided discharges. The second set of experiments consisted of 94-GHz Mach-Zehnder interferometer measurements of the conductivity of both laser-guided and exploding-wire discharges.

2

EXPERIMENTAL DETAILS

The NRL laser-guided discharge facility and setup is shown in Figure 1. The discharge was guided by a Nd:glass-laser-ionized channel in smoke-seeded laboratory air at atmospheric pressure and was terminated on a grounded graphite block. After the laser was fired, a fixed energy (350 kV, 1 kJ) Marx bank and a variable energy (0-4 kJ) slow capacitor bank were discharged along the laser channel to create a small diameter, very hot channel that hydrodynamically expanded in approximately 100 μs to a pressure-equilibrated channel several centimeters in diameter. Turbulent mixing of the hot channel also occurred on this time scale, and therefore, at late times (>100 μs) the channel consisted of regions of hot and cold gas. The length of the discharge was about 175 cm. Our measurements were made close to the end wall of the discharge; the 35-GHz measurements were made 30 cm from the end wall and the 94-GHz measurements 15 cm from the end wall.

The 35-GHz interferometer setup is schematically shown in Figure 2. The yoke assembly allowed for vertical y motion; thus, chord integrated measurements of attenuation and phase shift as a function of radial offset, y, were made. The interferometer mixing and detection setup, shown in Figure 3, was identical to that used in experiments at the Lawrence Livermore National Laboratory's advanced test accelerator (ATA) facility [SWE88].

The 94-GHz interferometer is shown schematically in Figure 4. It employed essentially the same horn configuration as in the 35-GHz interferometer setup, although focusing lenses were added to maximize coupling because power losses were severe at 94 GHz. We used a different mixing scheme (hybrid ring) for the 94-GHz setup to allow more efficient microwave power utilization. The interferometer mixing and detection setup for the 94-GHz interferometer is schematically shown in Figure 5.

Measurements of exploding-wire-initiated channels were made with the 94-GHz interferometer. The wire was approximately 40 cm long, 6.4×10^{-4} cm (0.00025 in.) in diameter, and the wire was fabricated from 304 stainless steel. The Marx bank and slow bank energies used were the same as those for the laser-initiated channels, although it should be noted that the discharge energy per unit length was significantly higher for the wire channels than for the laser channels because of the shorter discharge length with the
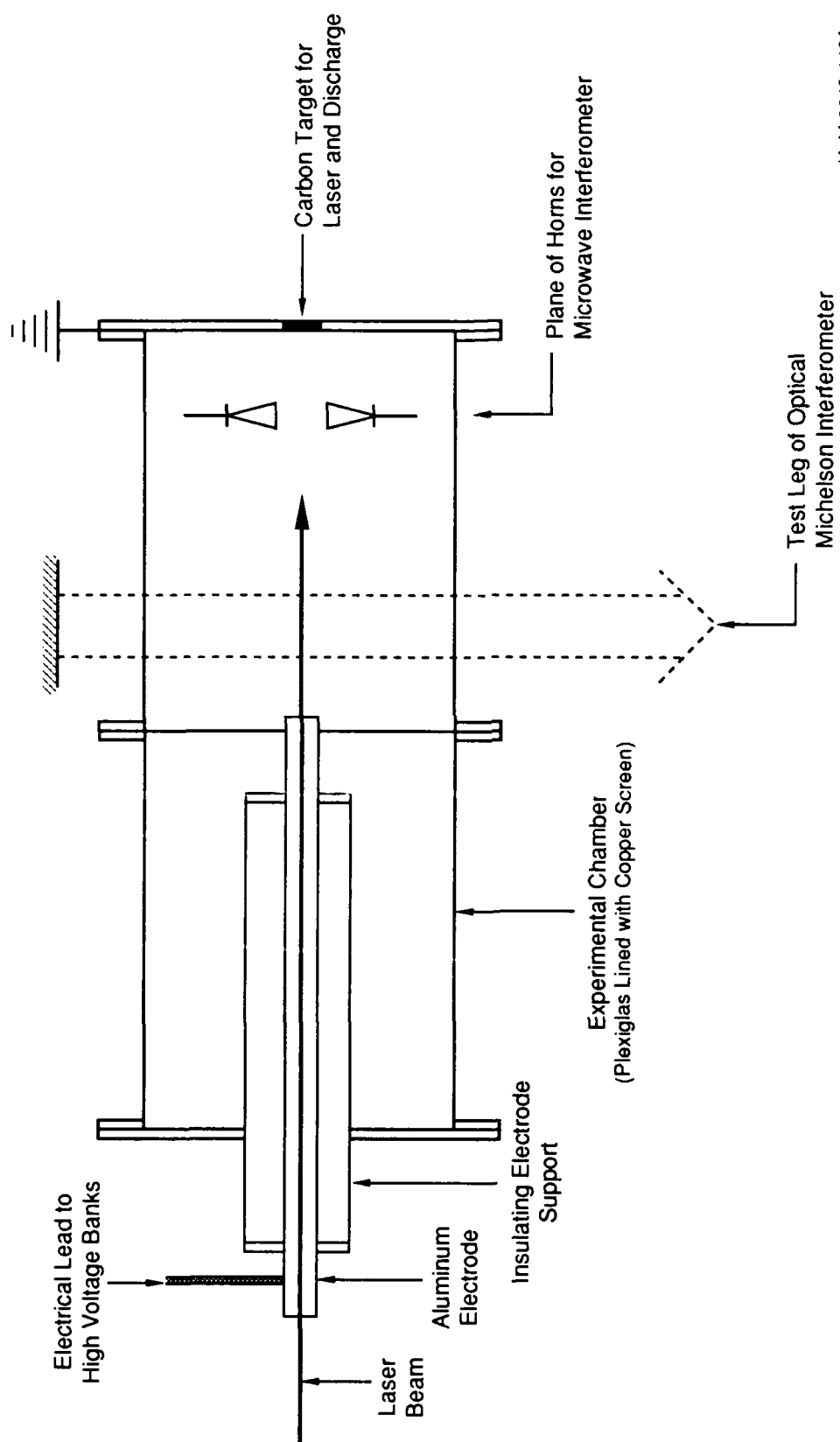
Figure 1. Schematic top view of experimental setup.

JA-M-8849-146A

4
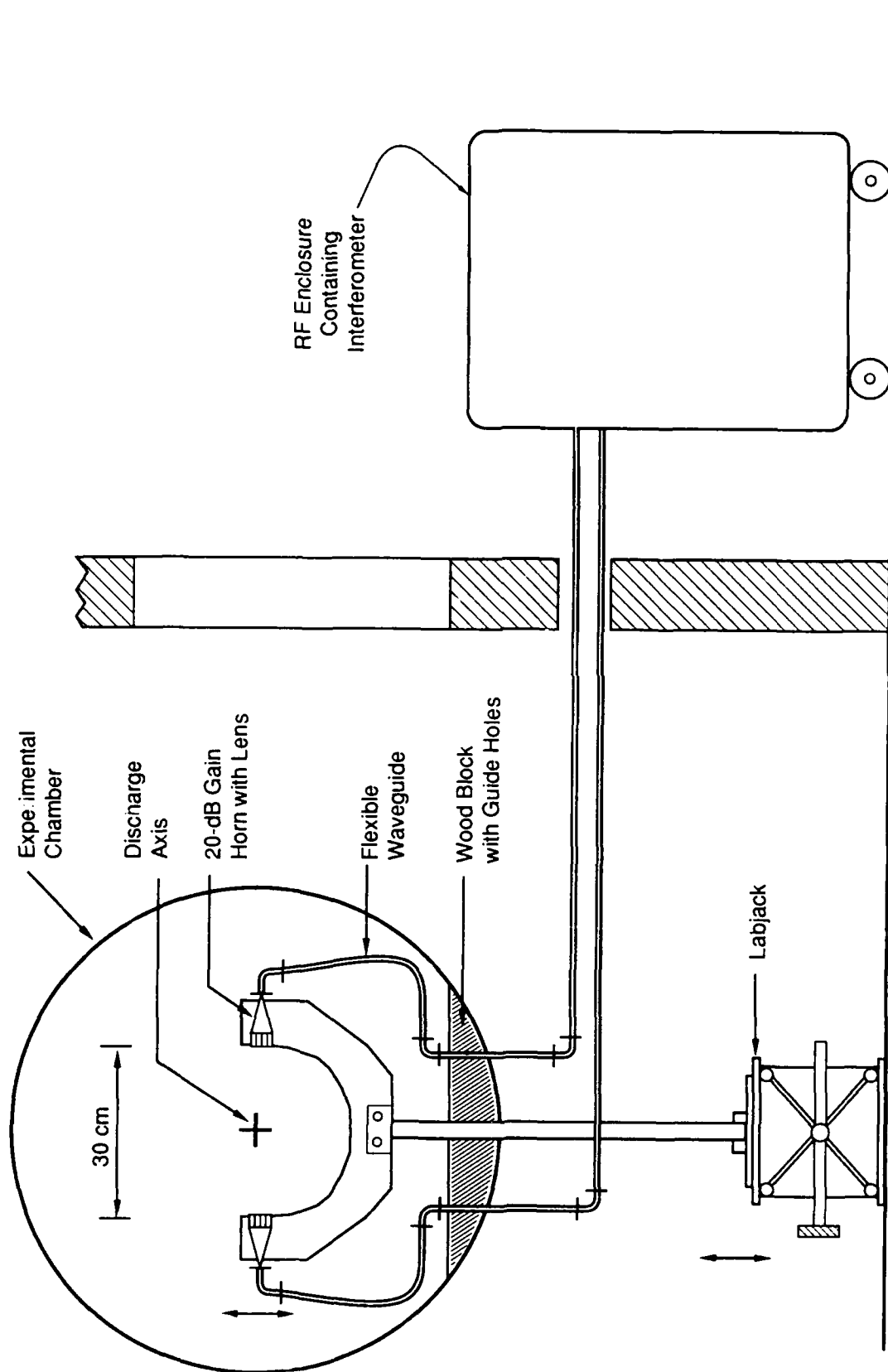
Figure 2. Schematic end view of 35-GHz microwave interferometer installed at NRL.

JA-M-8849-148A

RF Enclosure
Containing
Interferometer

Experimental
Chamber

Discharge
Axis

20-dB Gain
Horn with Lens

Flexible
Waveguide

Wood Block
with Guide Holes

Labjack

30 cm

5
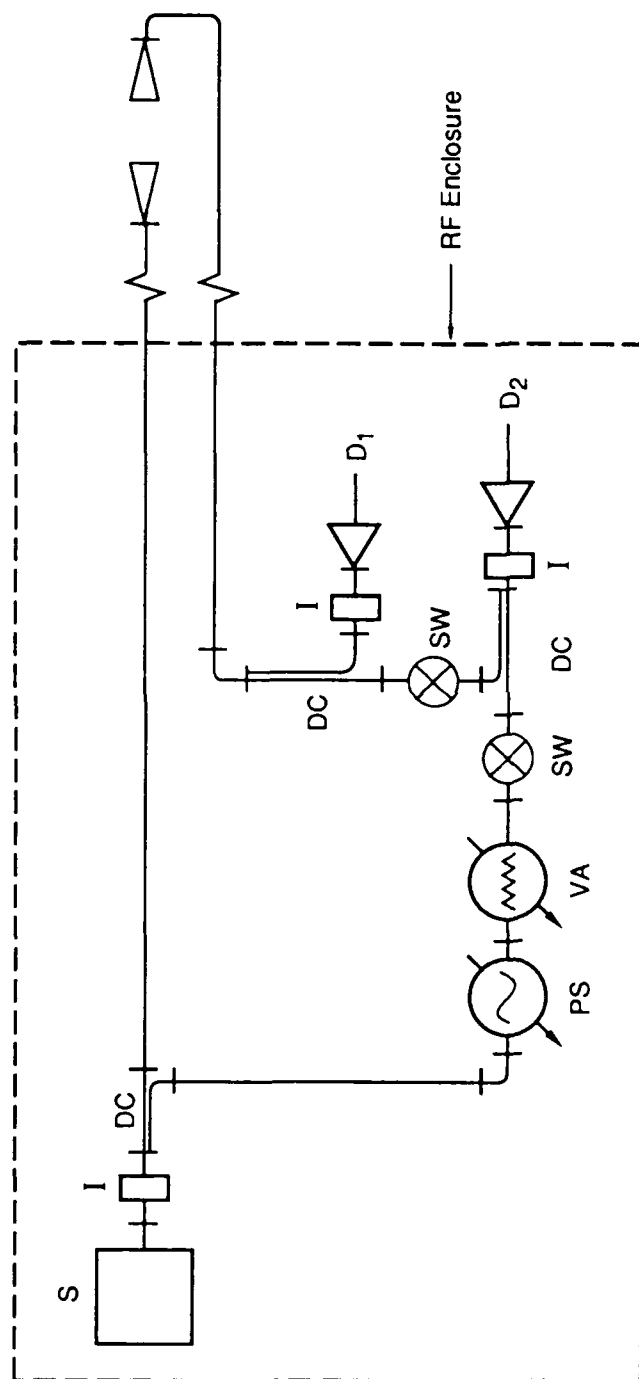
(S = Source, I = Isolator, DC = Directional Coupler, SW = Switch,
PS = Phase Shifter, VA = Variable Attenuator, D = Detector)

JA-M-8849-147A

Figure 3.   Schematic of 35-GHz microwave interferometer.

6

End Wall

RF Enclosure Containing Interferometer

16 cm

Labjack on Support Table

Antenna/Lens Support

Brace

Graphite Target for Laser and Discharge

SIDE VIEW

JA-M-8849-152A

Experimental Chamber

Discharge Axis

Slot for Antenna/Lens Support

30 cm

+y

15-dB Gain Horns with Collimating Lens on Kinematic Mount

Brace

END VIEW

Figure 4.   Schematic end view of 94-GHz microwave interferometer installed at NRL.

7

(S = Source, I = Isolator, DC = Directional Coupler, PS = Phase Shifter, VA = Variable Attenuator, EH = E-H Tuner, HR = Hybrid Ring, D = Detector, A = Video Amplifier, H = Horn Antenna, L = Collimating Lens.)

JA-M-8849-153A

Figure 5. Schematic of 94-GHz microwave interferometer.

8

wire channels. Most of the exploding-wire measurements were taken with 1-kJ Marx bank energy plus 2-kJ slow bank energy.

Initial checkout tests were performed using operating conditions for the channel typical of those used in previous NRL channel tracking studies [MTP88]. For the 35-GHz interferometer measurements, we found that discharges with 3.3 kJ slow bank energy arced to the yoke assembly when y was greater than +7 cm; we therefore limited our e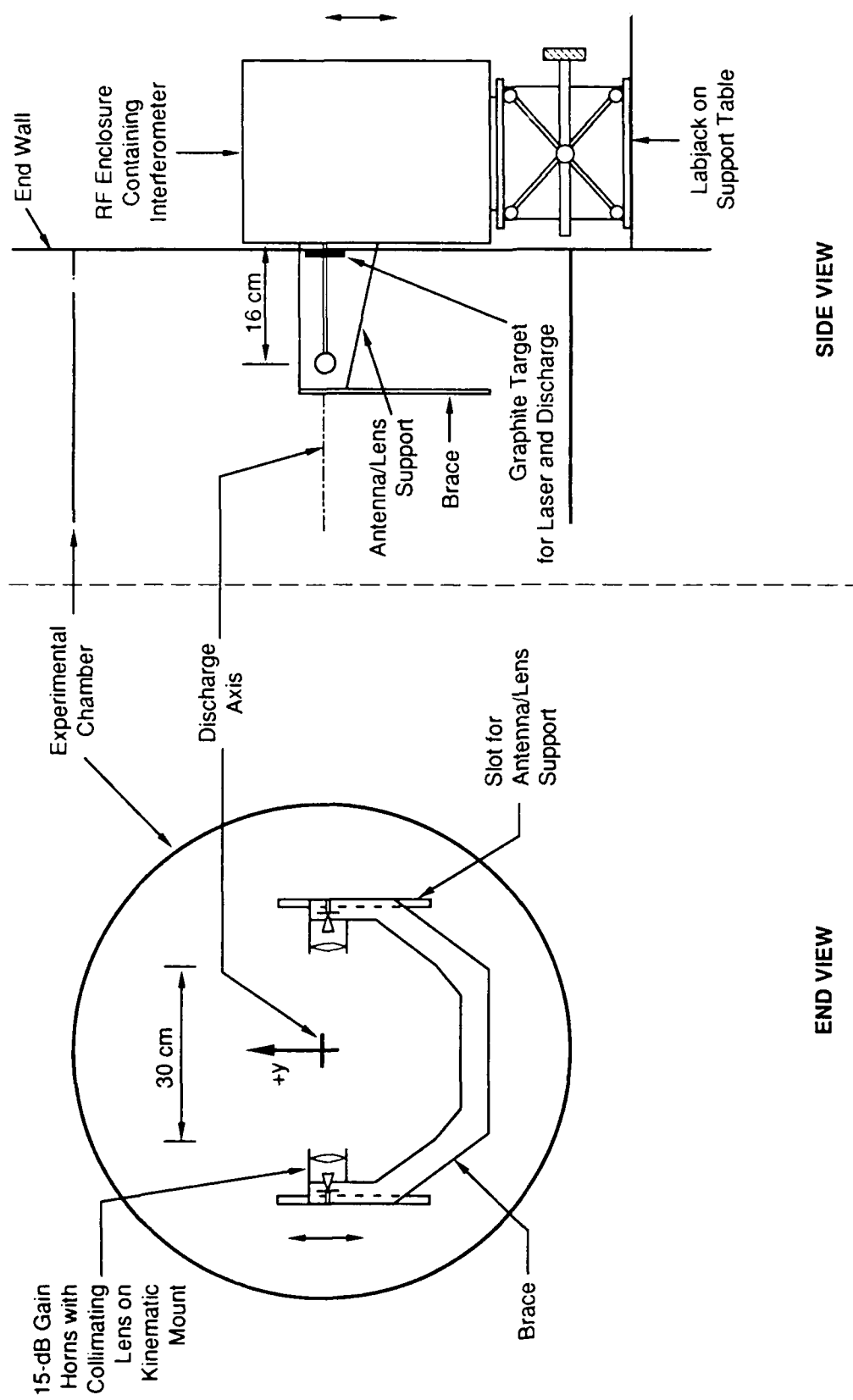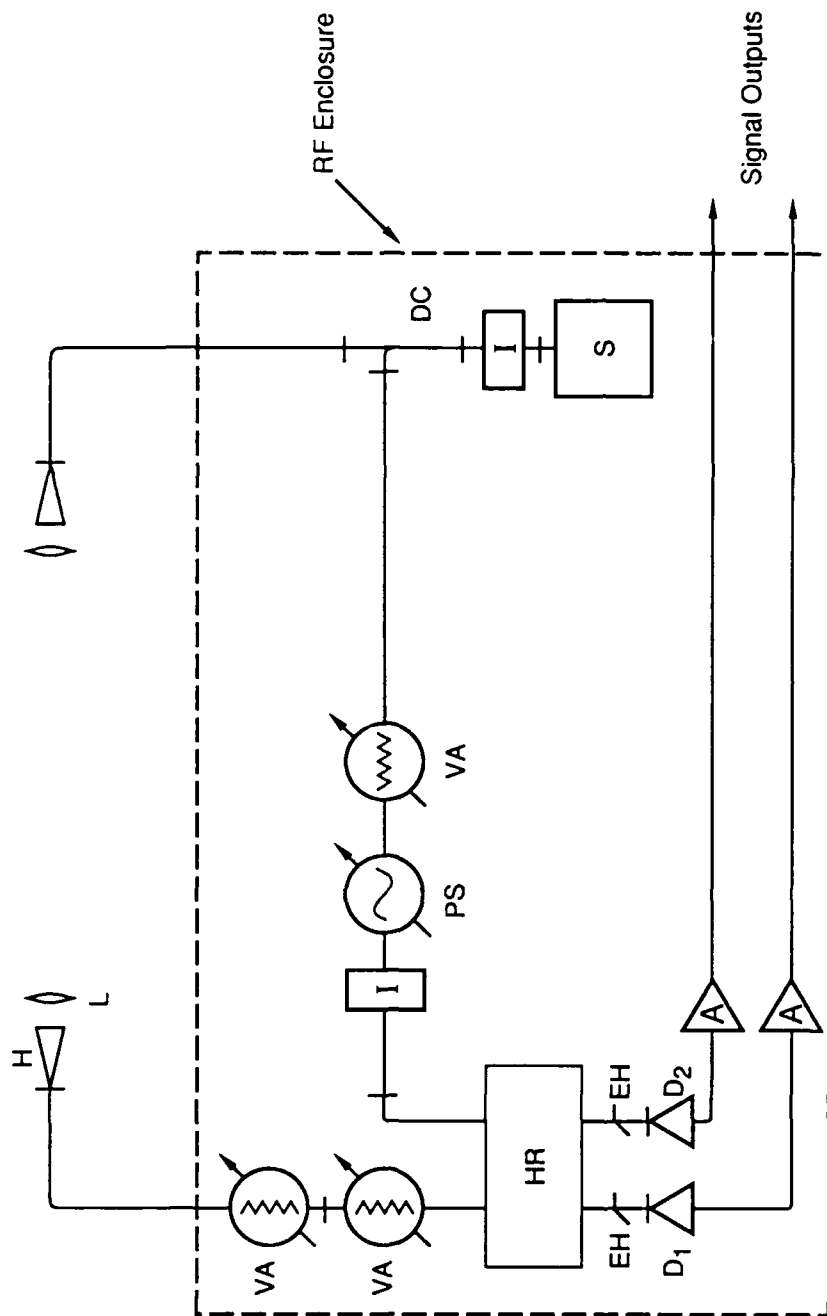xperimental measurements to y values less than +7 cm. Measurement conditions for all experiments are shown in Table 1. We ended the 35-GHz checkout tests with a set of shots using y = 0 and slow bank energies of 2 and 4 kJ to test the shot-to-shot variation of the channel conductivity. Some 35-GHz measurements were also made with variable slow bank capacitance to check the effects of this factor on channel properties.

Table 1.
TEST CONDITIONS FOR 35-GHz AND 94-GHz MEASUREMENTS

Legend: L_{35} = 35-GHz measurements of laser-created channels
L_{94} = 94-GHz measurements of laser-created channels
W_{94} = 94-GHz measurements of exploding-wire-created channels

	Slow Bank Energy (kJ)			
y (cm)	0	1	2	4
0	L_{35} L_{94} W_{94}	L_{35} L_{94} W_{94}	L_{35} L_{94} W_{94}	L_{35} L_{94} W_{94}
±1.3	L_{35} L_{94}	L_{35} L_{94}	L_{35} L_{94} W_{94}	L_{35} L_{94}
±2.5	L_{35} L_{94}	L_{35} L_{94}	L_{35} L_{94} W_{94}	L_{35} L_{94}
±3.8	L_{35} L_{94}	L_{35} L_{94}	L_{35} L_{94} W_{94}	L_{35} L_{94}
±5.1	L_{35} L_{94}	L_{35} L_{94}	L_{35} L_{94} W_{94}	L_{35} L_{94}
-6.4	L_{35}	L_{35}	L_{35}	L_{35}

DATA ANALYSIS

BASIC EQUATIONS

The basic principles of the measurement method are described in various books [HW65, MK73] and our previous reports [EDS85, SWE88]. The data analysis consists of calculating from the interferometer signals the phase shifts and field attenuation coefficients from which the real and imaginary conductivities may be computed. We summarize the basic equations below.

The complex electrical conductivity, $\hat{\sigma}$, of a plasma may be expressed as

$$\hat{\sigma} = -\frac{4\pi}{3} \frac{n_e e^2}{m_e} \int_0^\infty \frac{1}{\nu_e + j\omega} \frac{df_0(v)}{dv} v^3 \, dv \tag{1}$$

where e and m_e are the charge and mass of the electron, respectively, and n_e is the plasma density. This expression can be evaluated for arbitrary microwave frequency, ω, and variation of the electron collision frequency, ν_e, with v if the electron velocity distribution, $f_0(v)$, is known. Usually the distribution is assumed to be Maxwellian, in which case the real and imaginary conductivities can be calculated as a function of the electron temperature, T_e, for arbitrary ω and gas pressure. If one further assumes that ν_e is a constant, the conductivity can be written simply as

$$\hat{\sigma} = \sigma_r + j\sigma_i = \frac{\varepsilon_0 \omega_p^2}{(\nu_e + j\omega)} \tag{2}$$

or

$$\sigma_r = \frac{\varepsilon_0 \omega_p^2 \nu_e}{(\omega^2 + \nu_e^2)} \tag{3}$$

and

$$\sigma_i = \frac{-\varepsilon_0 \omega_p^2 \omega}{(\omega^2 + \nu_e^2)} \tag{4}$$

where $\omega_p^2 = \frac{e^2 n_e}{\varepsilon_0 m_e}$ is the square of the electron plasma frequency, which is a function of n_e; ν_e is now the effective electron collision frequency, which is a function of electron temperature; and ε_0 is the permittivity of free space [$\varepsilon_0 = (4\pi)^{-1}$ in cgs units].

10

The complex conductivity determines a complex dielectric constant for the plasma. This complex dielectric constant determines the attenuation and phase shift of a microwave probe beam. Because an interferometer measures phase shifts and attenuations, the complex dielectric constant and the complex conductivity may then be determined.

The complex dielectric constant allows us to define propagation constants for the microwave beam that determine the wavelength of the beam in the plasma and the attenuation coefficient of the beam. These constants are defined as μ and χ, respectively, and it can be shown that they are related to the complex conductivity by the following equations:

$$\begin{Bmatrix}\mu \\ \chi\end{Bmatrix} = \frac{1}{\sqrt{2}}\left\{ \pm\left(1 + \frac{\sigma_i}{\varepsilon_0\omega}\right) + \left[\left(1 + \frac{\sigma_i}{\varepsilon_0\omega}\right)^2 + \left(1 + \frac{\sigma_r}{\varepsilon_0\omega}\right)^2\right]^{1/2}\right\}^{1/2} \qquad (5)$$

These equations may be inverted to yield

$$\sigma_r = (2\mu\chi)\,\varepsilon_0\omega \qquad (6)$$

and

$$\sigma_i = (\mu^2 - \chi^2 - 1)\,\varepsilon_0\omega \qquad (7)$$

The phase shift, $\Delta\phi$, and field attenuation coefficient, α, of the microwave probe beam are related to the propagation constants by the following relations:

$$\Delta\phi = 2\pi L(1 - \mu)/\lambda \qquad (8)$$

and

$$\alpha = \chi\omega/c \qquad (9)$$

where L is the plasma pathlength, λ is the free-space wavelength of the microwaves ($\lambda f = c$), and c is the speed of light in vacuum ($c = 3 \times 10^{10}$ cm/s). Interferometric measurements of the phase shifts and attenuations thus determine μ and χ, from which the complex conductivities may be computed.

Once σ_r and σ_i are determined, one can solve for the plasma frequency, ω_p, and electron collision frequency, ν_e, using Equations (3) and (4).

It should be noted that the above conductivities are AC conductivities at the microwave probe frequency used. Conductivities relevant to electron beam propagation are DC values, where

11

$$\sigma_{DC} = \frac{\varepsilon_0 \omega_p^2}{\nu_c} \qquad (10)$$

These DC values must be calculated from Equation (10) once the values of ω_p and ν_c have been determined as outlined above.

ANALYSIS OF THE 35-GHz INTERFEROMETER SIGNALS

The analysis of the 35-GHz interferometer data uses the directly measured scene signals and interference signals to derive the complex conductivity. The detector voltage signals are converted to microwave power through the use of measured calibration curves. The field attenuation coefficient, α, is derived from the transmitted power, $P_t(t)$, by using

$$\alpha = \frac{1}{2L} \ln\left[\frac{P_t(t=0)}{P_t(t)}\right], \qquad (11)$$

where $P_t(t=0)$ is the transmitted power in the absence of a plasma. For these plasmas, the plasma pathlength, L, is a function of y and *a priori* is unknown. We initially choose an arbitrary value (in this case, 10 cm), and then use the Abel inversion (see Appendix A) to determine the true plasma pathlength.

The phase shift is derived from the interference power, P_i, and the transmitted power, P_t, according to the relation

$$P_i = P_t + P_r + 2(P_t P_r)^{1/2} \cos(\phi_t - \phi_r), \qquad (12)$$

where P_r is the power transmitted in the reference leg and $\phi_t - \phi_r$ is the relative phase between the transmitted and reference legs. This equation can be rewritten to yield an expression for the phase change

$$\Delta\phi = \cos^{-1}\left\{\frac{P_i(t) - P_t(t) - P_r}{2[P_t(t)P_r]^{1/2}}\right\} \qquad (13)$$

μ and χ are then determined by substituting Equations (11) and (13) into Equations (8) and (9). Once μ and χ have been determined, the complex conductivities are determined from Equations (6) and (7) and the DC conductivity is from Equation (10).

12

We found that for many measurement conditions, the 35-GHz microwaves were totally attenuated until several milliseconds after the laser pulse. This attenuation implies that the conductivity during this period was very high. Because some power must be transmitted through the scene leg for the interferometer to measure a phase shift, the strong attenuation limited our analysis of the data. However, we took an alternative approach and used just the attenuation data to determine lower bounds for the conductivity by assuming equilibrium air conditions. The equilibrium air calculations are described below.

ANALYSIS OF THE 94-GHZ INTERFEROMETER SIGNALS

The analysis of the 94-GHz data required using different equations for the attenuation and phase shift since a different interference mixing component was used. The hybrid mixer splits the microwave power from the reference and scene legs equally and recombines the power onto two detectors. The microwave power split from one leg, e.g., the reference leg, also is phase shifted $180°$ with respect to that from the other leg. Thus, the incident power on the detectors, P_1 and P_2, obeys the following relations [OSH87]:

$$P_1 = 2P_r + 2P_t + (P_r P_t)^{1/2} \cos(\Delta\phi) \tag{14}$$

and

$$P_2 = 2P_r + 2P_t - (P_r P_t)^{1/2} \cos(\Delta\phi) \tag{15}$$

With $(t=0)$ defining the start of the discharge, and the interferometer initially set so that $P_r = P_t$, we have

$$P_r = 1/2 \ [P_1(t=0) + P_2(t=0)] \tag{16}$$

$$P_t(t) = 1/2 \ [P_1(t) + P_2(t)] \tag{17}$$

and

$$\cos[\Delta\phi(t)] = \frac{[P_1(t) - P_2(t)]}{2[P_r P(t)]^{1/2}} \tag{18}$$

Once the scene power histories and phase shift histories are obtained, the rest of the data analysis follows exactly the same procedures as outlined above for the 35-GHz interferometer. Even though the 94-GHz microwaves usually were not totally attenuated like the 35-GHz microwves, we also used equilibrium air calculations to analyze the 94-GHz data.

13

EQUILIBRIUM AIR CALCULATIONS

Although the complex conductivities could be calculated directly from the phase shifts and attenuations when the microwaves were not totally attenuated, we found it useful to analyze the data by alternative techniques as well. In fact, since the Abel inversion yielded the on-axis value of the attenuation coefficient or phase shift, we used that information to determine the on-axis conductivity, assuming that equilibrium air conditions were applicable. This procedure allowed us to assess the contribution of contaminants on the conductivity. The two methods described in the preceding sections were used to compute the DC conductivity solely from the attenuation data or solely from the phase shift data. Equilibrium air calculation also determines the channel temperature, a useful parameter for characterizing the degree of density reduction.

The equilibrium air calculations are based on Saha equilibrium calculations of the electron density for dry synthetic air (80% N_2 and 20% O_2) as a function of temperature. The electron collision frequency is computed by integrating momentum transfer cross sections over a Maxwellian electron energy distribution in equilibrium with the gas temperature. This procedure results in a collision frequency that is a function of the temperature. These values then determine theoretical curves showing attenuation coefficients, α, phase shifts, $\Delta\phi$, and DC conductivities, σ_{DC}, as functions of temperature. Thus, measurements of the microwave attenuation or phase shift can be used to determine the temperature and corresponding DC conductivity of equilibrium air.

Curves for the theoretical equilibrium air attenuation, phase shift, and DC conductivity are shown in Figures 6 through 8.
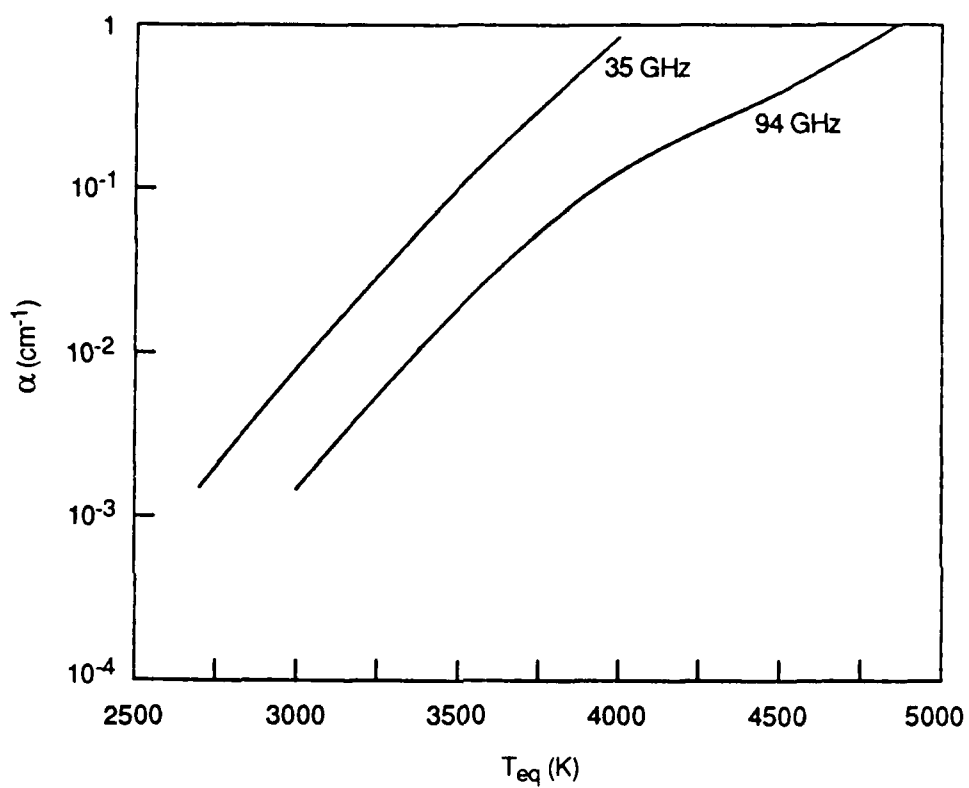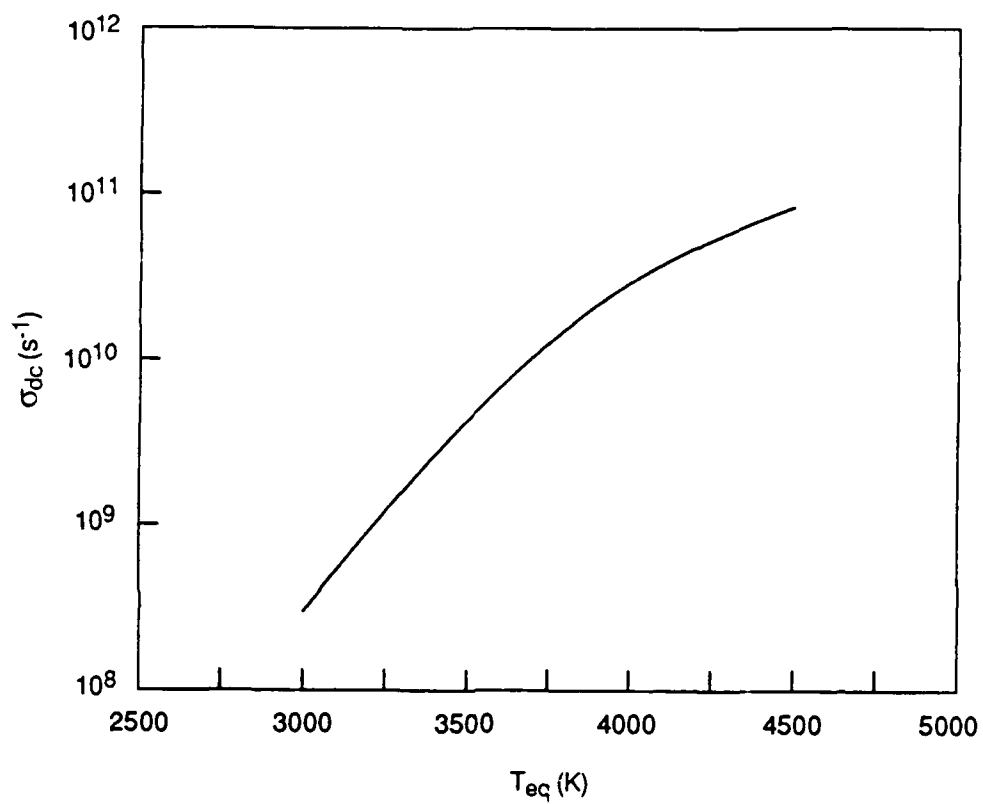
Figure 6.   Microwave absorption for equilibrium air at P=760 Torr.

15
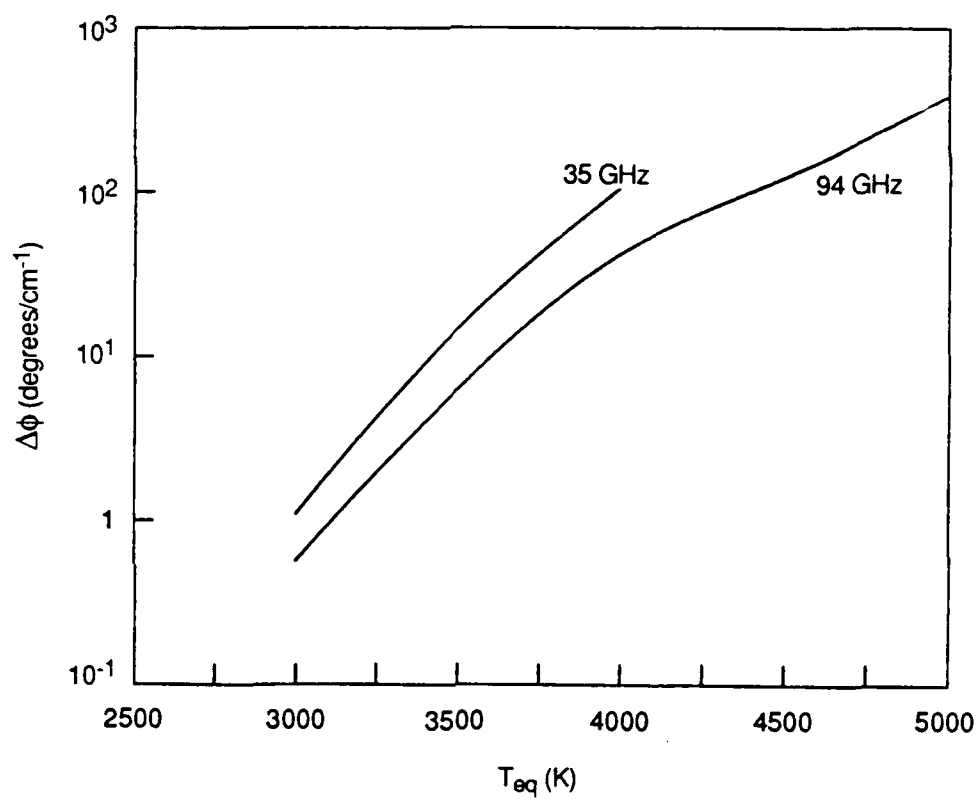
Figure 7. Microwave phase shift for equilibrium air at P=760 Torr.

JA-8849-163

Figure 8. DC conductivity for equilibrium air at P=760 Torr.

JA-8849-164

17

RESULTS

Typical transmitted and interference signals from the 35-GHz interferometer are shown in Figure 9. Note that the transmitted signal appears totally attenuated for more than 2 ms. It is difficult to determine the attenuation coefficient accurately when the power attenuation is significantly greater than about 13 dB. We could, however, make lower bound estimates of the attenuation coefficients whenever the signals were so severely attenuated. For the channel radii of these experiments, an on-axis value of $\alpha = 0.4$ is about the maximum measurable for the 35-GHz microwaves; this corresponds to equilibrium temperatures of 3600 K or equilibrium DC conductivities of 2×10^{10} s^{-1}.

There also was significant shot-to-shot variation in the data, as illustrated in Figure 10. To illustrate the data averaging and analytic fits, we present the entire 35-GHz attenuation data set in Appendix B. These data were Abel inverted using the methods described in Appendix A; the resulting on-axis attenuation coefficients and Figures 6 and 8 were then used to determine equilibrium DC conductivities. We followed this same procedure for the 94-GHz interferometer data. The equilibrium DC conductivities determined by this method for both the 35-GHz and 94-GHz measurements are shown in Figures 11 and 12.

The 35-GHz and 94-GHz phase shift data were also reduced to equilibrium DC conductivities by the same techniques. The resultant equilibrium DC conductivities are shown in Figures 13 and 14.

The equilibrium DC conductivity determined from the 35-GHz interferometer data generally is lower than that determined from the 94-GHz interferometer data. We believe that the main cause of this difference is that the 35-GHz interferometer was totally attenuated for many combinations of y and slow bank energies, whereas the 94-GHz interferometer in most cases was never totally attenuated. However, the 94-GHz interferometer was not as sensitive to lower conductivity levels ($< 10^{10}$ s^{-1}), so the results from the 35-GHz interferometer are more accurate at those levels.
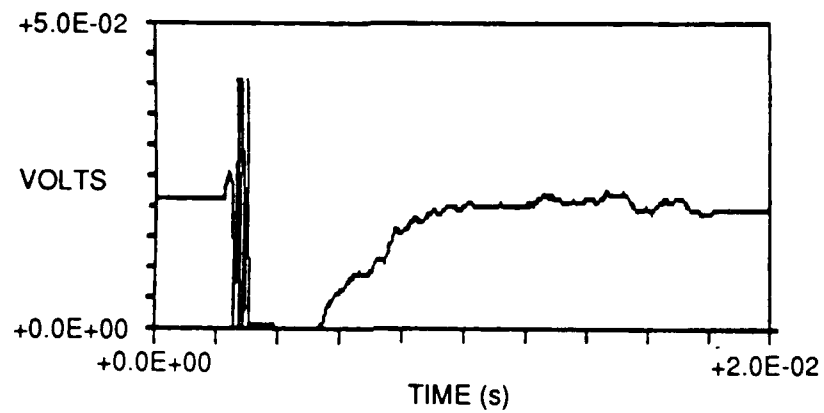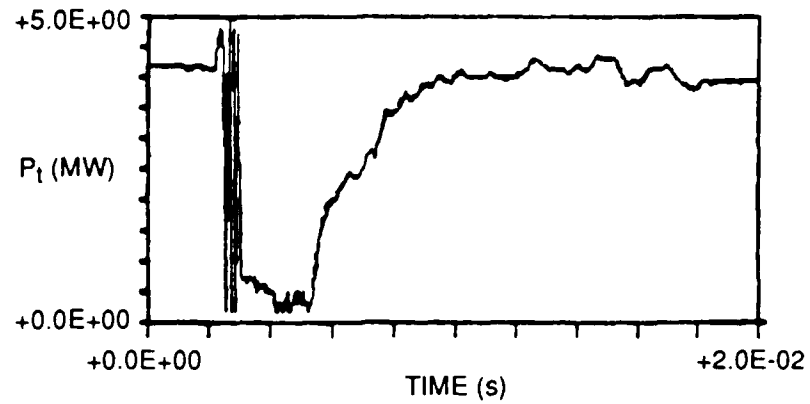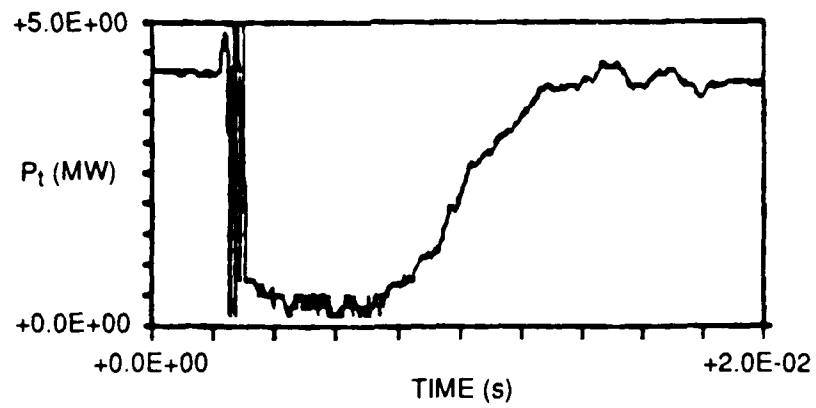
(a) Transmitted Signal
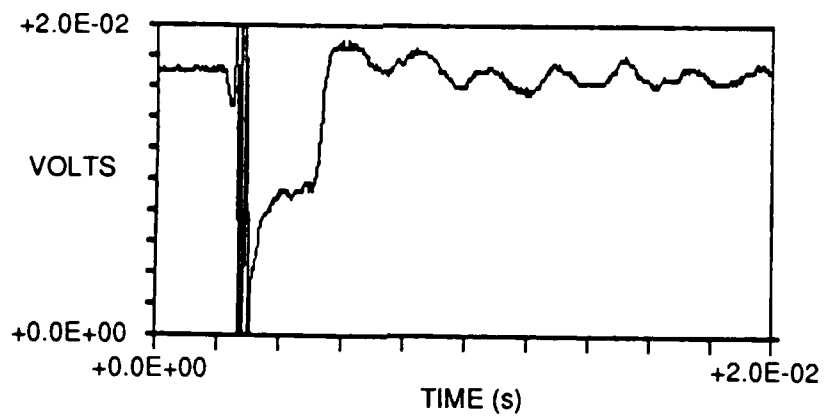
(b) Interference Signal

JA-8849-165

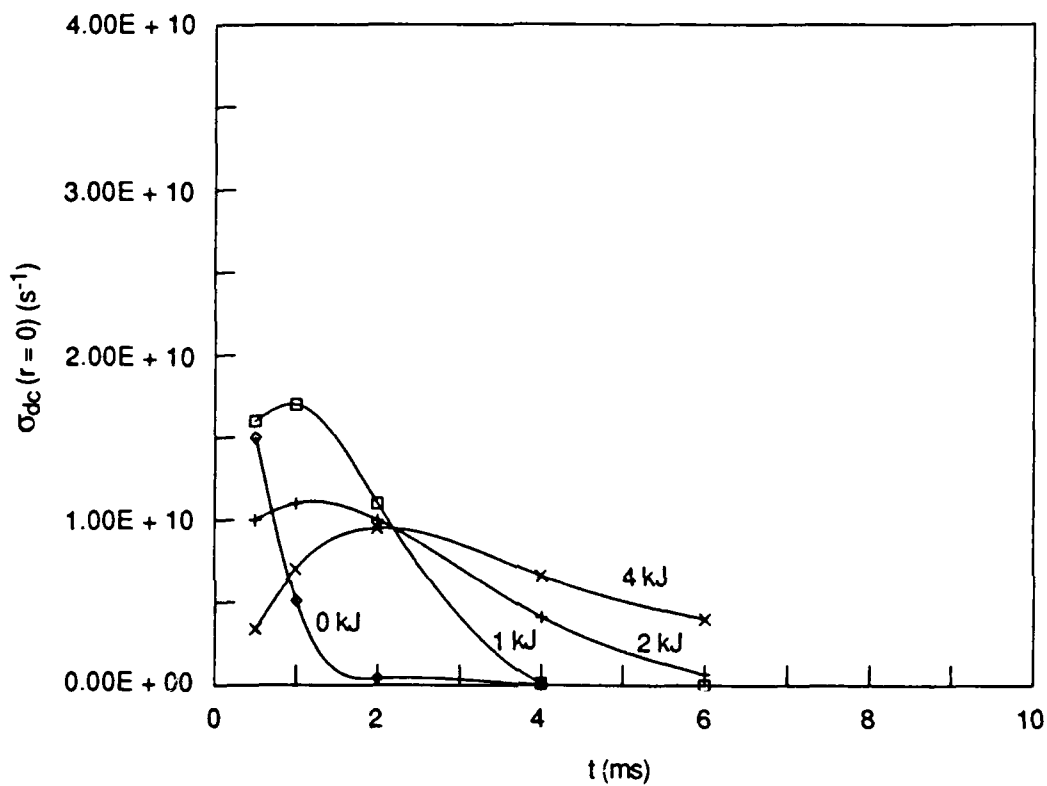Figure 9. Transmitted and interference signals versus time.

19

(a) Shot 168

(b) Shot 167
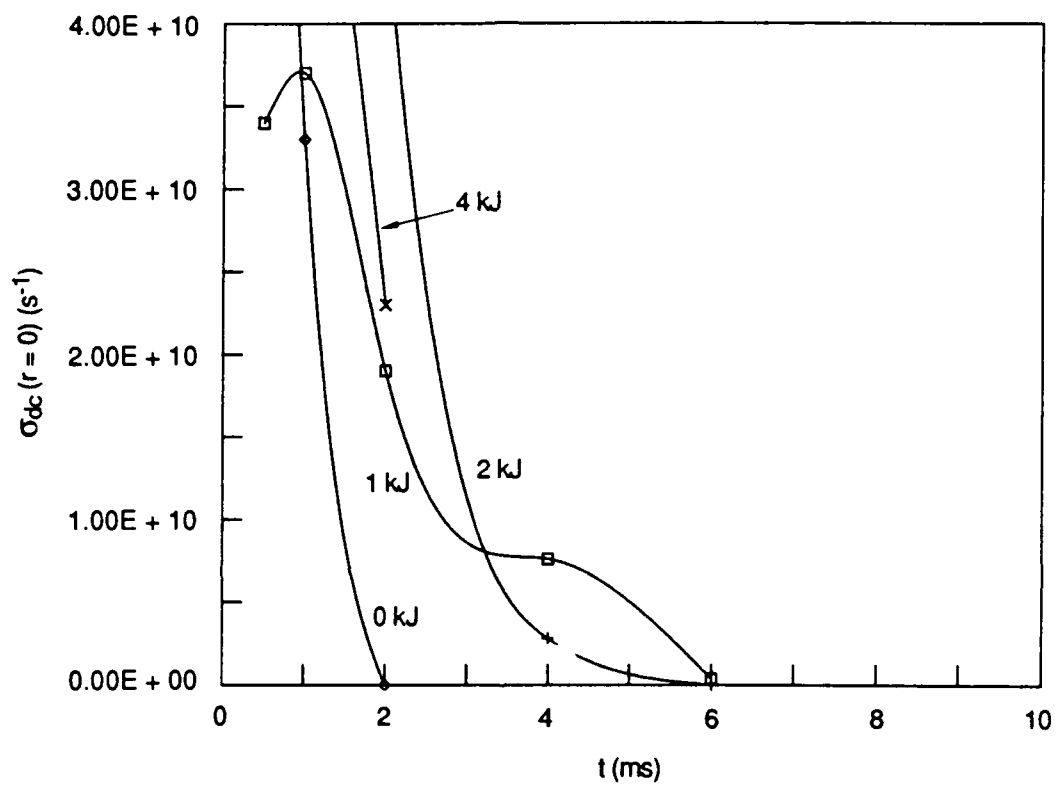
JA-8849-166

Figure 10.   Example of the shot-to-shot variation.

20

Figure 11. DC conductivity based on 35-GHz attenuation, assuming equilibrium air.

JA-8849-167

$\sigma_{dc}(r=0)$ (s^{-1})

4.00E + 10

3.00E + 10

2.00E + 10

1.00E + 10

0.00E + 00

4 kJ

1 kJ

2 kJ

0 kJ

0   2   4   6   8   10

t (ms)
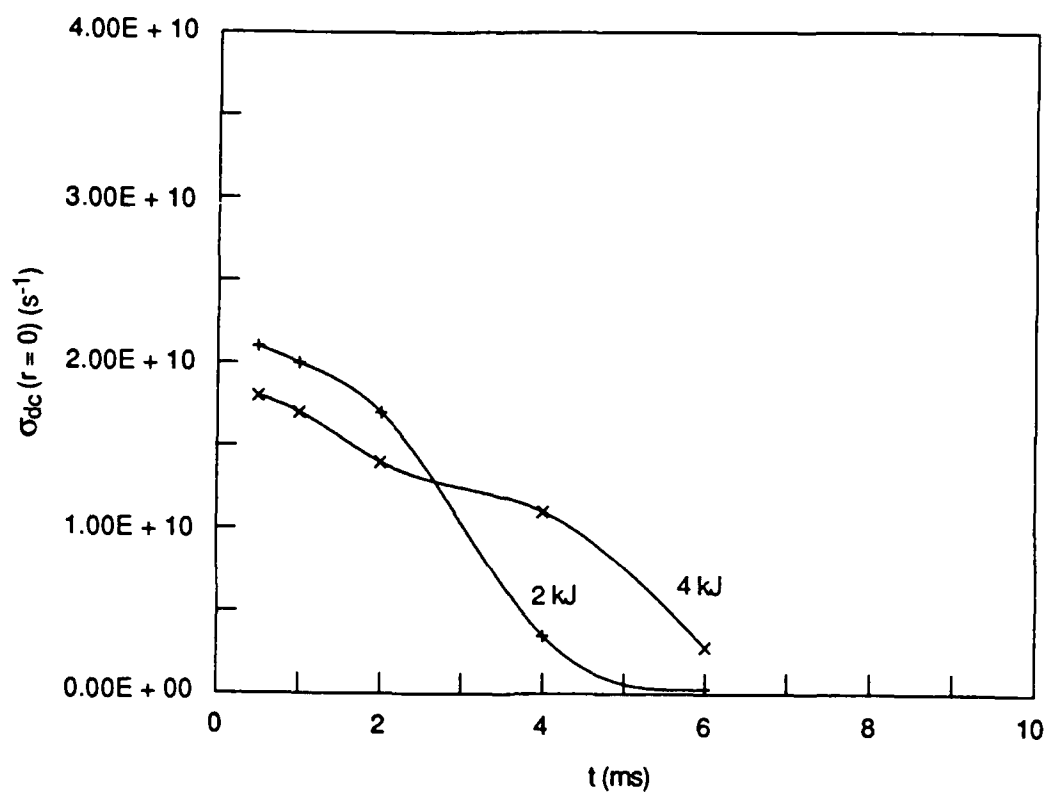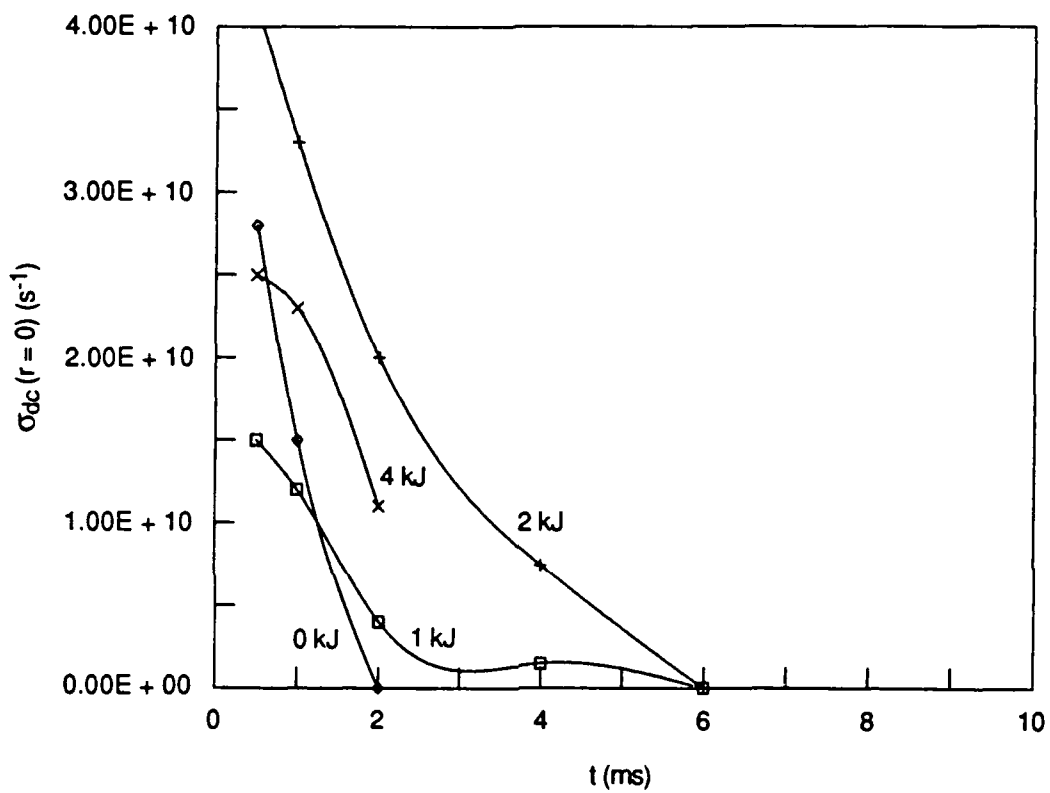
JA-8849-168

Figure 12.   DC conductivity based on 94-GHz attenuation, assuming equilibrium air.

22

Figure 13. DC conductivity based on 35-GHz phase shifts, assuming equilibrium air.

Figure 14. DC conductivity based on 94-GHz phase shift, assuming equilibrium air.
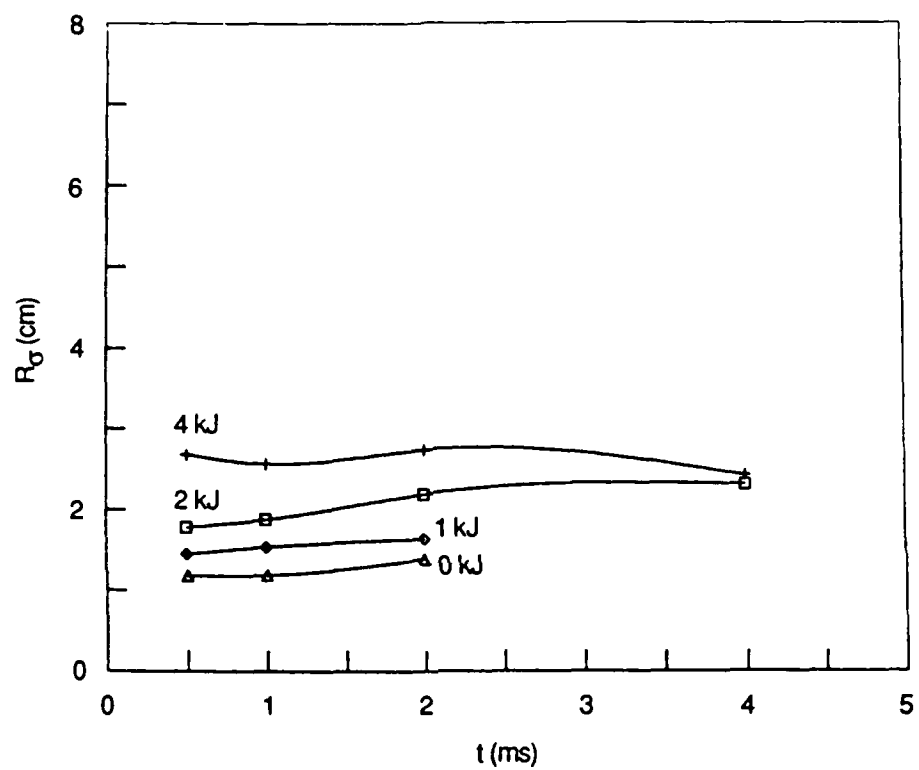
JA-8849-170

24

The phase shift measurements at the two frequencies are generally in better agreement than the attenuation measurements, because refraction effects tend to enhance the measured attenuation, i.e., to make it greater than that due to true microwave absorption, and refraction was more severe at 35 GHz. The measured phase shifts take into account all sources of attenuation (both absorption and refractive losses) of the transmitted beam. Refractive losses increase the apparent absorption anbd thus imply erroneously large conductivities if just the equilibrium air absorption method is used.

The channel radii determined by Abel inversion of the 35-GHz attenuation measurements are shown in Figure 15, and those determined by Abel inversion of the 94-GHz attenuation measurements are shown in Figure 16. For comparison, the channel radii measured by the NRL optical interferometer are shown in Figure 17 [Pe88]. There is good quantitative agreement between the microwave-derived channel radii, but these are somewhat smaller than those measured by the optical interferometer. This difference is due to the optical interferometer's sensitivity to neutral density changes that are not detectable with the microwave interferometer. Turbulent mixing of the edge of the channels probably cools the interface to such levels that the conductivity is not measurable with microwaves, but density changes are easily measured with the optical interferometer.

The most direct method of determining the conductivity without using the equilibrium air assumptions is to use the Abel-inverted channel diameter to iteratively re-analyze the transmitted and interference power data into real and imaginary conductivities and hence DC conductivity. Once this is done, it is possible to compare the actual DC conductivity to the equilibrium DC conductivity and in this way assess the role of contaminants (the role of contaminants is considered in the Discussion, below).

Examples of the recomputed time histories of the DC conductivity for individual shots measured with the 94-GHz interferometer are shown in Figures 18 through 21. Each graph is for a different slow bank energy. The recomputed DC conductivities from data obtained with the 94-GHz interferometer averaged over several shots, are shown in Figures 22 through 25.

Finally, the Gaussian radius for the exploding-wire shots measured with the 94-GHz interferometer is shown in Figure 26. The DC conductivity of the exploding-wire discharges, assuming equilibrium air, is shown in Figure 27.
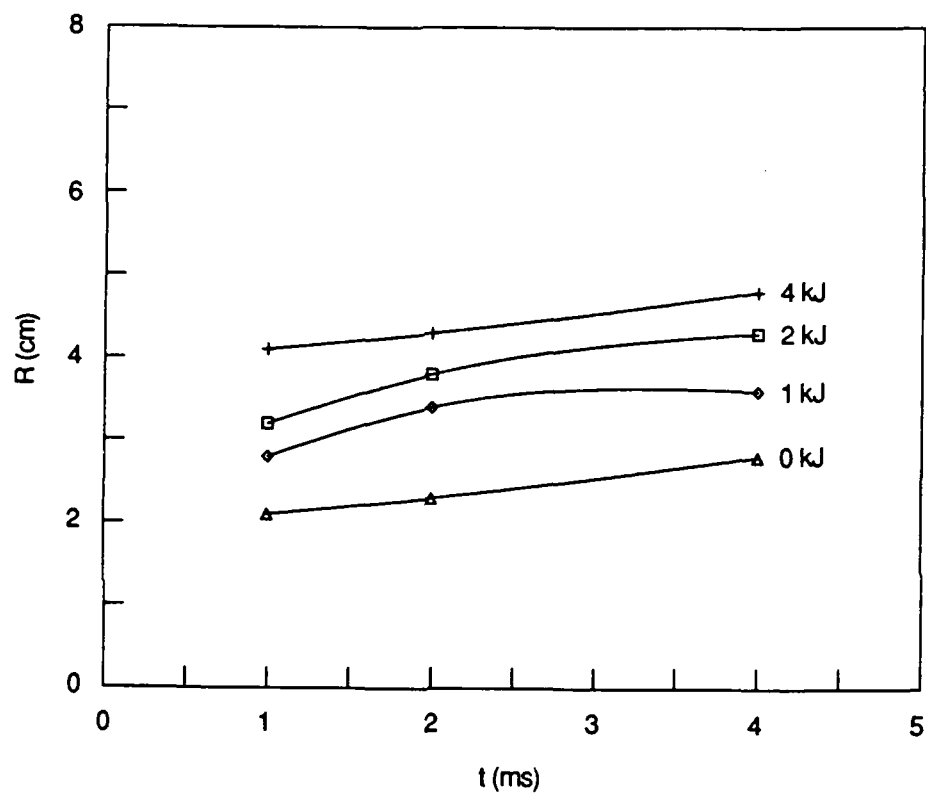
Figure 15. Mean Gaussian conductivity radius based on 35-GHz absorption.
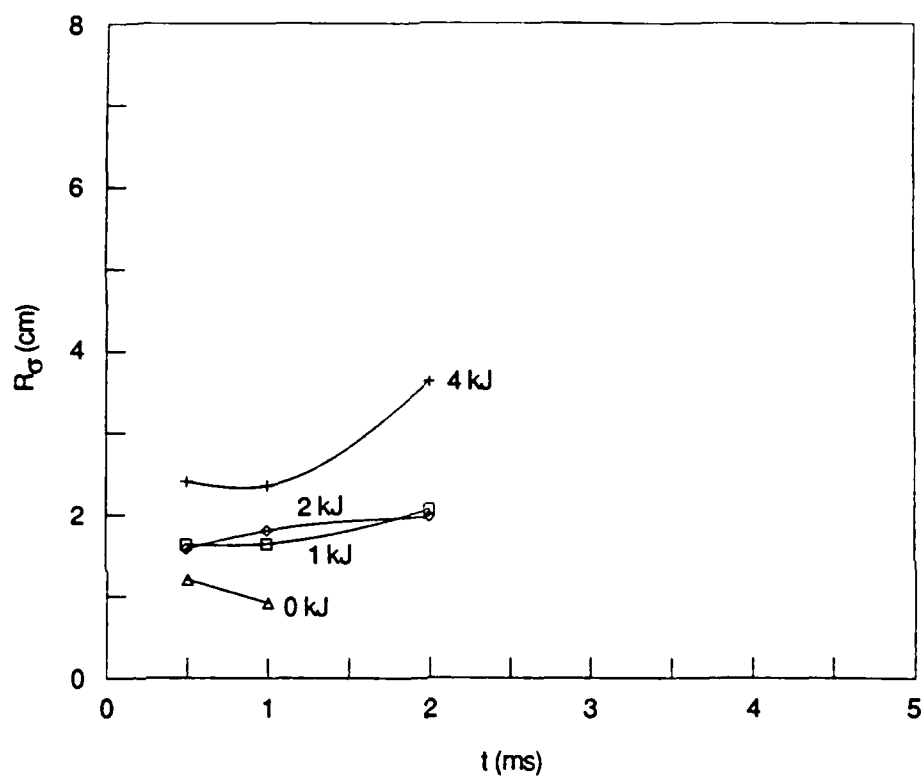
JA-8849-171

Figure 16. Mean Gaussian conductivity radius based on 94-GHz absorption.

JA-8849-172

27

JA-8849-173

Figure 17.   Density channel radius measured by optical interferometer.

28

+5.0E+09

σ_{DC} (s^{-1})

+0.0E+00

+0.0E+00   +1.0E-02

TIME (s)
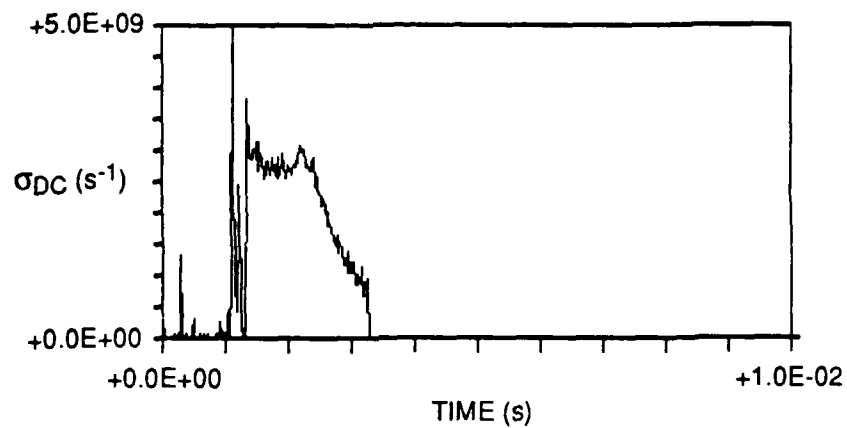
JA-8849-174A

Figure 18.   Single-shot DC conductivity using radius determined from
             Abel inversion of 94-GHz data (0 kJ).
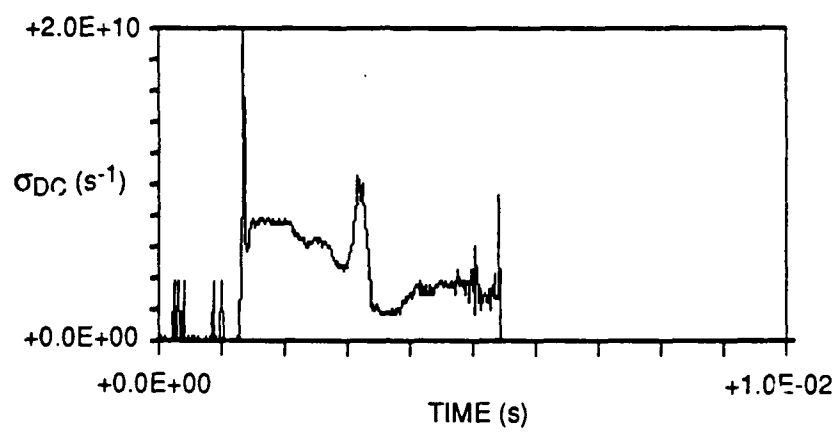
Figure 19. Single-shot DC conductivity using radius determined from Abel inversion of 94-GHz data (1 kJ).

JA-8849-174B

30

+2.0E+10

σ_{DC} (s^{-1})

+0.0E+00

+0.0E+00   +1.0E-02

TIME (s)
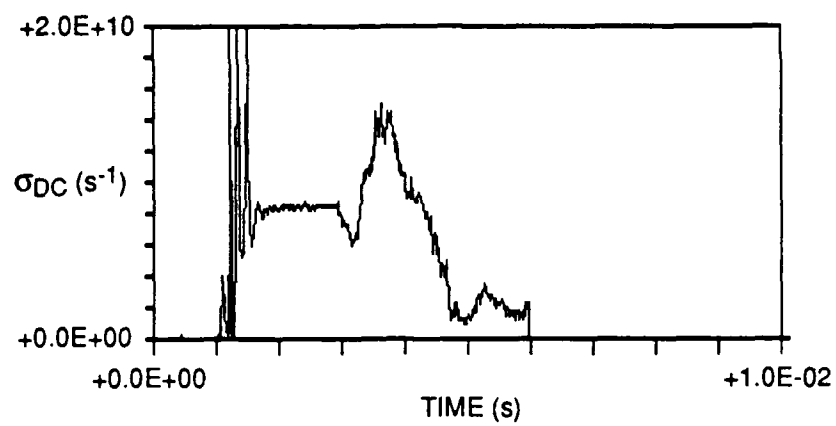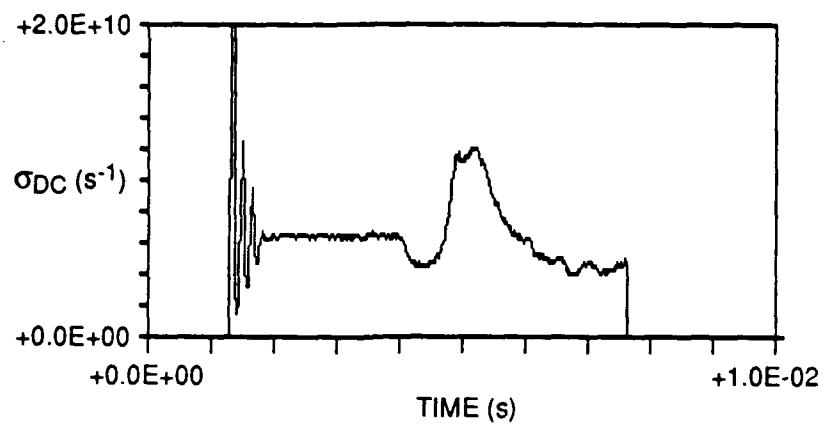
JA-8849-176A

Figure 20. Single-shot DC conductivity using radius determined from
Abel inversion of 94-GHz data (2 kJ).

+2.0E+10

σ_{DC} (s^{-1})

+0.0E+00

+0.0E+00   +1.0E-02

TIME (s)

Figure 21. Single-shot DC conductivity using radius determined from Abel inversion of 94-GHz data (4 kJ).

The y-axis is labeled $\sigma_{dc}(r=0)\ (s^{-1})$ with values 0.00E+00, 1.00E+10, 2.00E+10, 3.00E+10, 4.00E+10. The x-axis is labeled $t\ (ms)$ with values 0, 2, 4, 6, 8, 10. The curve is labeled 94 GHZ.
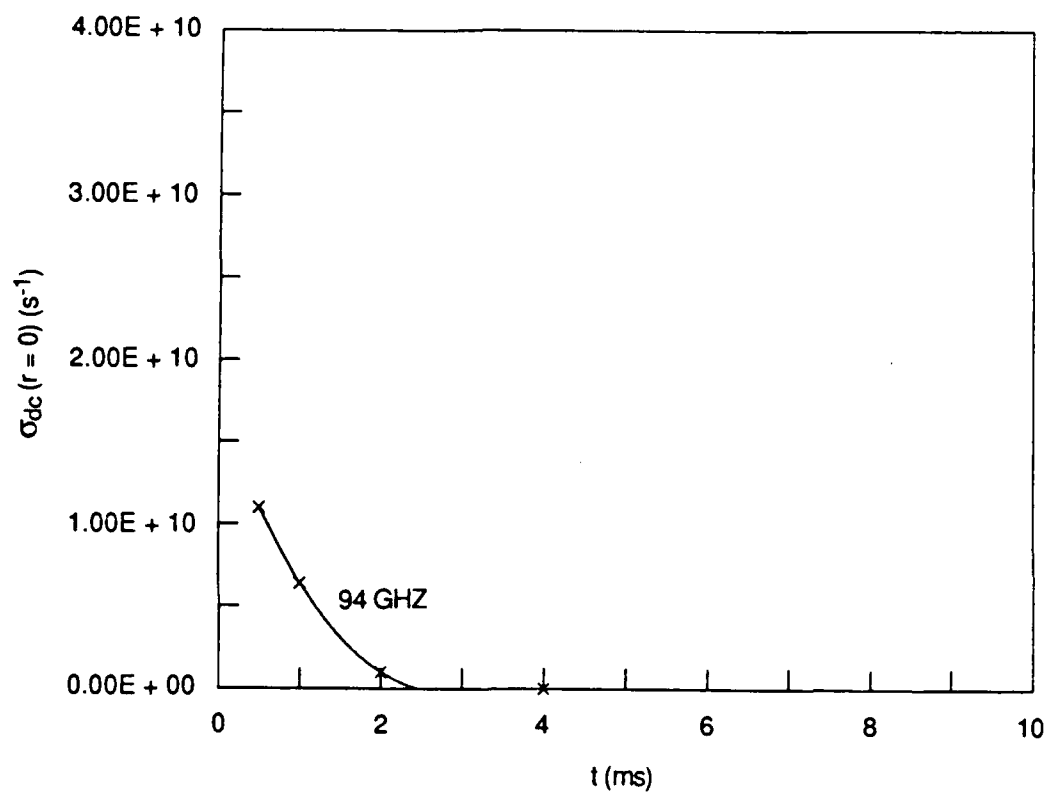
JA-8849-178

Figure 22. On-axis DC conductivity derived from n_e and v_e (0-kJ slow bank).

33
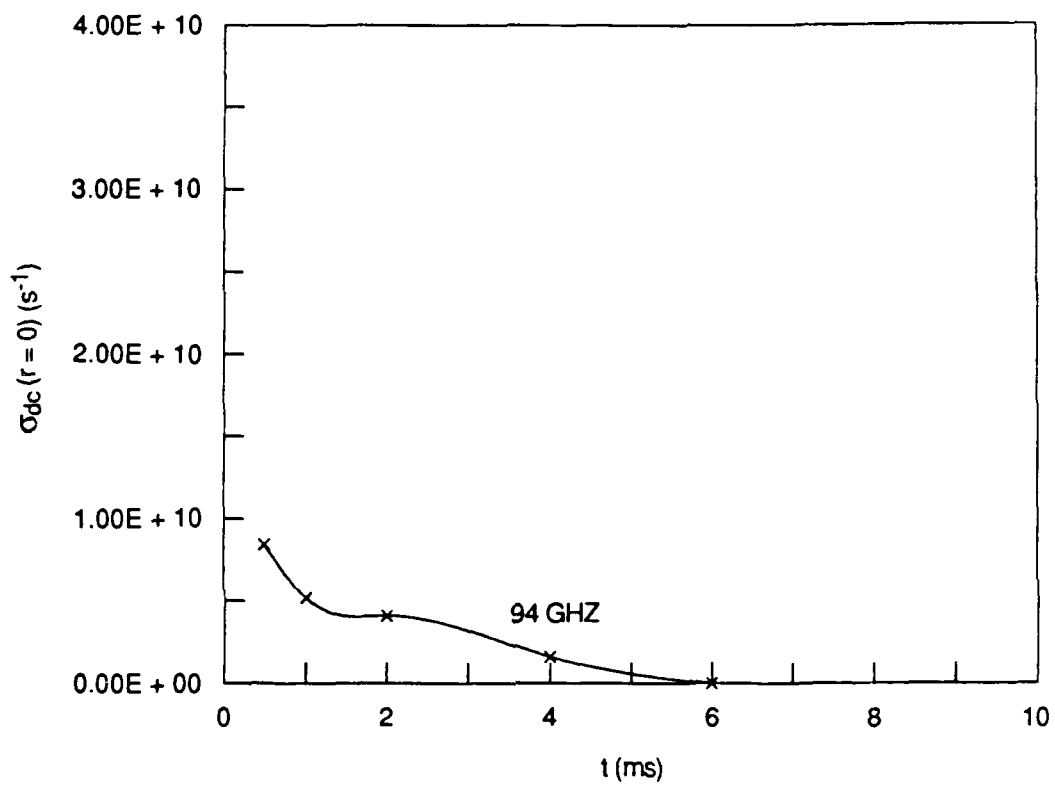
Figure 23.   On-axis DC conductivity derived from n_e and ν_e (1-kJ slow bank).

JA-8849-179

y-axis label: σ_{dc} (r = 0) (s^{-1})

x-axis values: 0, 2, 4, 6, 8, 10

y-axis values: 0.00E + 00, 1.00E + 10, 2.00E + 10, 3.00E + 10, 4.00E + 10

label on curve: 94 GHZ

x-axis label: t (ms)

JA-8849-181

Figure 24.   On-axis DC conductivity derived from n_e and ν_e (2-kJ slow bank).
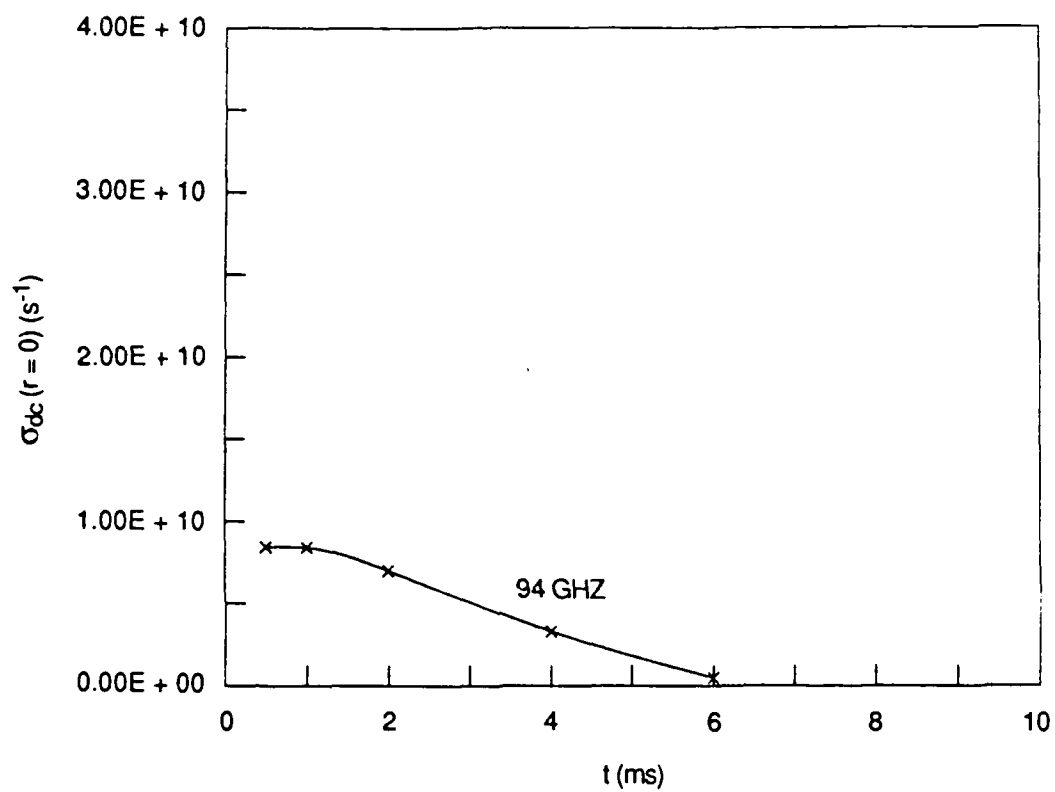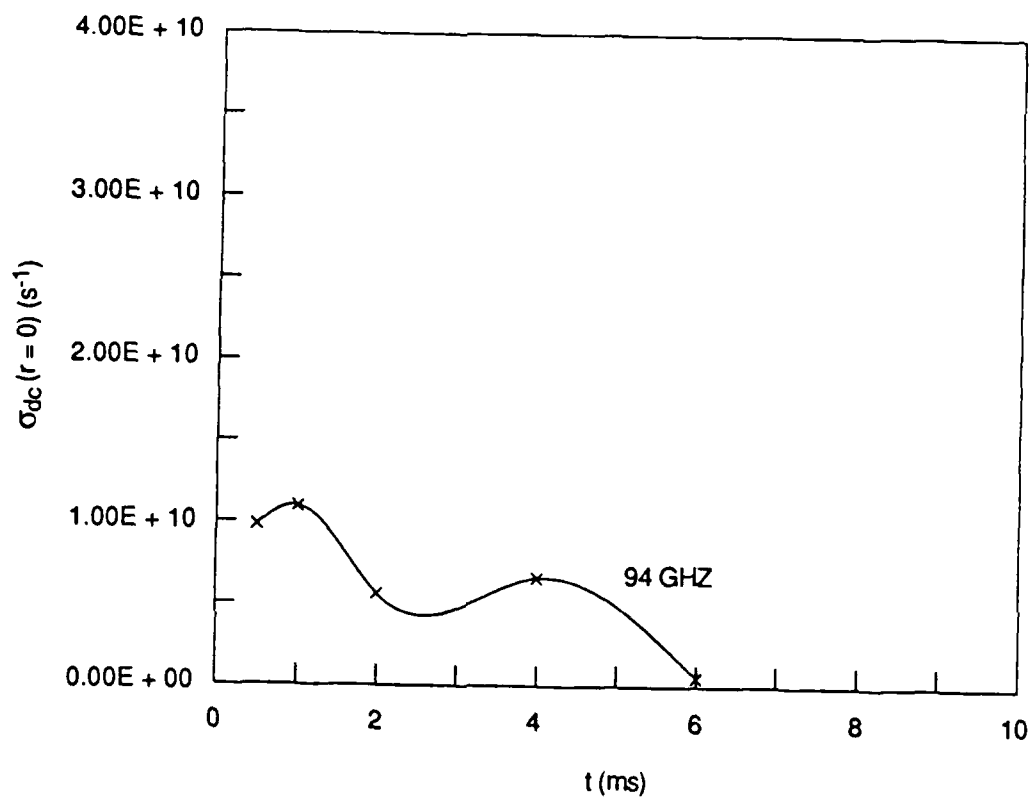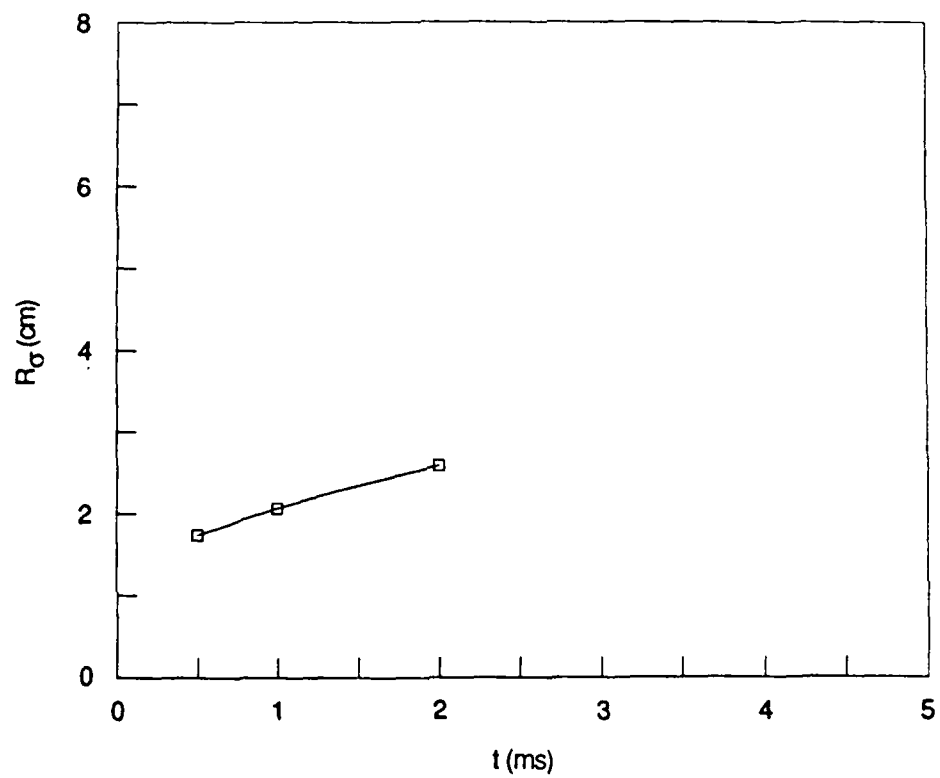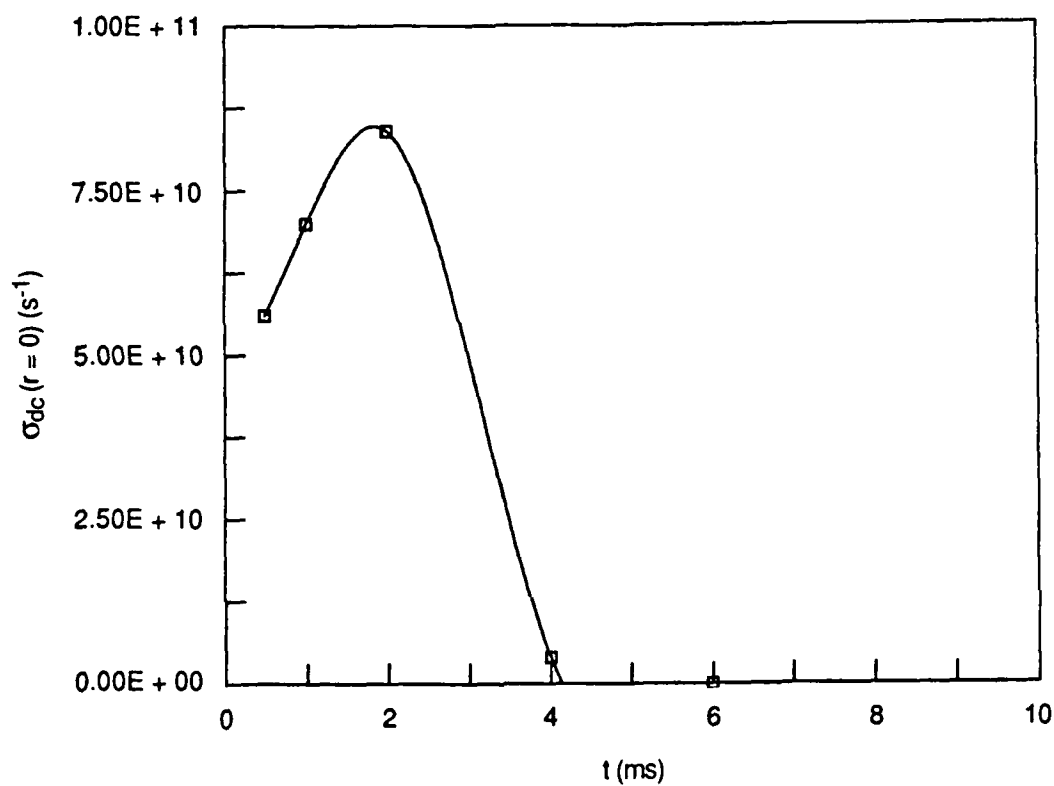
Figure 25. On-axis DC conductivity derived from n_e and v_e (4-kJ slow bank).

Figure 26.   Gaussian radius for exploding wire (1 kJ Marx + 2 kJ slow bank).

JA-8849-182

Figure 27. DC conductivity for exploding wire assuming equilibrium air (1 kJ Marx + 2 kJ Slow bank).

JA-8849-183

DISCUSSION

LASER-GUIDED DISCHARGES

The measurements from the 35-GHz and 94-GHz interferometers are in good agreement over their common range of sensitivities. On the centerline, the 35-GHz microwaves were strongly attenuated for much of the afterglow period, and this attenuation resulted in inaccurate measurements of the conductivity. The 94-GHz microwaves were not as strongly attenuated, and thus the conductivities derived from those measurements are more accurate. However, the lower sensitivity of the 94-GHz interferometer made conductivity measurements late in the afterglow less accurate; the 35-GHz measurements were more accurate at late times.

The DC conductivities determined from the measurements of phase shifts and assumed equilibrium air reached a peak at $2\text{-}5 \times 10^{10}$ s^{-1}, which corresponds to equilibrium temperatures of up to 4000 K. Three milliseconds after the Marx bank fired, the conductivity ranged from 4×10^8 s^{-1} with 0 kJ slow bank energy to 7×10^9 s^{-1} with 4 kJ slow bank energy. We also note that, after an initial blackout period due to noise, the attenuation almost invariably increased, reaching a local maximum one to several milliseconds after the laser firing. This is exemplified in Figure 10b, where the attenuation is larger at 4 ms than it is at 1 ms. We believe that this is a real effect, because it was observed with both the 35-GHz and 94-GHz interferometers. The most likely explanation for this observation is that the ringing discharge current continues to dump energy into the channel for several hundred microseconds. There may also be a transfer of energy from internal molecular energy reservoirs [for instance, metastable $N_2(A)$] to the electrons that enhances their ionization rate and thus increases the conductivity. The DC conductivity computed from both the real and imaginary conductivities, without the assumption of equilibrium air, peaked at 1×10^{10} s^{-1}. The lower level of conductivity based on both the collision frequencies and electron densities probably is related to the effects of contaminants. The most likely contaminants would be from the exploded gunpowder aerosol, and these would be carbon-containing species like CO, CO_2, CH, and so forth. These species generally have lower ionization potentials than O_2 or N_2, and thus should

tend to enhance the electron density and therefore the conductivity, but our observations show a lower conductivity. Thus, the lower conductivity most likely is due to a significantly higher electron collision frequency rather than a lower electron density [see Equation (10)]. For electron temperatures below 10 eV, the electron-neutral collision frequency increases with increasing temperature. Because the DC conductivities derived from the equilibrium air assumption typically are a factor of 2 to 4 larger than those calculated from both n_e and v_e, the electrons must have a collision frequency at least this much higher.

The contaminants would be very low in density. For example, a 10-μm diameter particle contains approximately 4×10^{13} atoms; one fully dissociated particle per centimeter would create a contaminant density of approximately 6×10^{11} cm^{-3} in a fully expanded channel of 5-cm radius. Even this low density may lead to significantly larger electron density if the ionization potential is low. However, the presumed higher collision frequency cannot be explained by the contaminant density. The contributions of water vapor, NO and electron-ion collisions [P72] are probably much higher and probably account for the larger-than-equilibrium collision frequencies and the lower-than-equilibrium DC conductivities.

The conductivity was sometimes observed to increase significantly 2-4 milliseconds after the Marx bank fired (see Figures 19 through 21, for example). There are several possible causes for this increase. It could be due to the interchange of hot and cold gas regions in the measurement region. It could also be the result of gas heating due to the returning shock wave that originated from the pre-expanded discharge channel and reflected from the Plexiglas wall of the experimental chamber. In fact, on several occasions we saw clear evidence of sharp conductivity increases coinciding with the returning shock (round-trip time approximately 2.8 ms). The averaged results from many centerline measurements, shown in figures 22 through 25, does not show a strong tendency for conductivity increases late in time, so hot-gas/cold-gas interchange, which should average out for statistical reasons, appears to be the best explanation for this observation.

Channel tracking is predicted at conductivity levels of 5×10^9 s^{-1}; our results show that these conductivity levels were reached in about 2-6 ms, depending on the slow bank energy. These results are in good agreement with NRL measurements of the conditions when channel tracking was observed [Mu88]. These experiments were not run concurrently with ours.

.

EXPLODING-WIRE DISCHARGES

The DC conductivity of the exploding-wire discharges was significantly higher than that of the laser-guided discharges. Because the discharge energy per unit length for the exploding-wire discharges was higher by about a factor of 5, this result is not surprising. For shots with a discharge of 75 J/cm (1-kJ Marx plus 2-kJ slow bank), the measured conductivity was as high as 10^{11} s^{-1} and dropped to the 5×10^9 s^{-1} level after about 4 ms. Recalling the lower sensitivity of the 94-GHz interferometer to conductivities of that level, we speculate that had we also made 35-GHz measurements for the exploding-wire discharges, we would have measured a longer time for the conductivity to drop to 5×10^9 s^{-1}, perhaps 6-8 ms.

Some beam tracking experiments using exploding wires have been tried at RADLAC at Sandia National Laboratory (SNL). Although the results did not conclusively show that there were positive tracking forces when the conductivity fell late in the afterglow [Fr88], they did show that the beam was ejected early in the discharge time, and this result is consistent with beam de-tracking at high conductivity levels. Unfortunately, we cannot directly compare the results of our NRL measurements with those of the SNL experiments because the conductivity was not directly measured in those SNL beam propagation studies.

CONCLUSIONS AND RECOMMENDATIONS

We measured conductivity levels in reduced density channels created by laser-initiated and exploding-wire-initiated electrical discharges at NRL.

The laser-initiated density channels expanded in several hundred microseconds, and cooled by adiabatic expansion and turbulent mixing. During the pressure equilibrium phase, we measured conductivity levels as high as 4×10^{10} sec^{-1}, corresponding to equilibrium temperatures of 4000 K or density reductions of approximately 90%. The channels cooled in millisecond time scales to conductivity levels of 5×10^9 sec^{-1}. For example, 4 kJ slow bank energy discharges took approximately 5 milliseconds to cool so that the conductivity was reduced to 5×10^9 sec^{-1}. Lower energy discharges took less time to reach that conductivity level.

The exploding-wire-initiated density channels started much hotter, due to their larger discharge energy per unit length, and cooled by the same mechanisms. The conductivity, as measured by our 94-GHz interferometer, was as high as 10^{11} sec^{-1}, and decreased to 5×10^9 sec^{-1} in 4 milliseconds. If we had used the more sensitive 35-GHz interferometer to measure the exploding-wire initiated density channels, we probably would have measured a longer time for the conductivity to decay to 5×10^9 sec^{-1}; we estimate 6-8 milliseconds.

These artificially produced reduced density channels are important for studying the propagation and stability of charged particle beams in the atmosphere since the reduced density channels are of the magnitude envisioned for very high current-density beams. However, impurities in the laser-initiated and exploding-wire-initiated channels probably cause different air chemistry to take place than would occur in electron-beam produced density channels, and thus the electrical conductivity of the artificially produced channels may be different than would occur in electron beam produced channels. The turbulence created by the discharge mechanisms probably drives a much higher level of turbulent mixing than would occur in electron beam produced density channels, and thus the cooling rate of electron beam produced channels would be expected to be much smaller.

We recommend that additional measurements of the conductivity levels of reduced density channels for new experimental conditions be made by microwave techniques, as

these measurements are shown to be effective, non-perturbing probes of electrical conductivity. As beam propagation experiments proceed to higher current densities, we advocate that further microwave interferometric measurements be made to firmly establish the relation of beam parameters to reduced density channel properties, so as to quantify the study of the stability and propagation of charged particle beams in such channels.

ACKNOWLEDGEMENTS

REFERENCES

[BJS60]   M. P. Bachynski, T. W. Johnston and I. P. Shkarofsky, *Proc.IRE*, **48**, 347 (1960).

[EDS85]   D. J. Eckstrom, J. S. Dickinson and M. N. Spencer, Diagnostics Development for E-Beam Excited Air Channels Technical Report No. 2, Conductivity Measurements on the Phermex Electron Beam. SRI Report No. 85-178 (July, 1985).

[Fr88]   C. A. Frost, private communication.

[HW65]   M. A. Heald and C. B.Wharton, *Plasma Diagnostics with Microwaves*, (J. Wiley and Sons, New York, 1965).

[JFF88]   E. E. Jones, C. A. Frost, J. R. Freeman, and J. M. Jojola, in *Proceedings of the Annual Propagation Physics Review of the Defense Advanced Research Projects Agency and of the Strategic Defense Initiative Organization and of Army, Navy and Air Force*, Monterey, (1988) p. 303 [Secret].

[MK73]   M. Mitchner and C. H. Kruger, Jr., *Partially Ionized Gases*, (Wiley-Interscience, New York, 1973).

[MRPG87]   D. P. Murphy, M. Raleigh, R. E. Pechacek and J. R. Greig, Phys. Fluids **30**, 232 (1987).

[MTP88]   D. Murphy, D. Taggert, R. Pechacek, M. Raleigh, M. Myers, M. Nash, and R. Meger, in *Proceedings of the Annual Propagation Physics Review of the Defense Advanced Research Projects Agency and of the Strategic Defense Initiative Organization and of Army, Navy and Air Force*, Monterey, (1988) [Secret].

[Mu88]   D. Murphy, 1988 Annual Propagation Review, Newport RI. Proceedings to be published.

[OSH87]   T. J. Orzechowski, E. T. Scharlemann and D. B. Hopkins, Phys.Rev. A **35**, 2184 (1987).

[P72]   A.V. Phelps, in *DNA Reaction Rate Handbook*, second edition, Chapter 21 (Defense Nuclear Agency, Washington, DC, 1972).

[Pe88]   R. E. Pechacek, Private Communication.

[SWE88]   K. R. Stalder, M. S. Williams, and D. J. Eckstrom, Propagation
Diagnostics Measurements, Microwave Diagnostics of the ATA Electron
Beam Propagating in Air. SRI Report No. 88-213 (August, 1988).

45

APPENDIX A

ABEL INVERSION

ABEL INVERSION

The microwave interferometers measure chord integrated values of α and $\Delta\phi$. We assume that the system is cylindrically symmetric. Then, with the coordinate system shown in Figure A-1, the measured attenuation is

$$\bar{\alpha}(y)L = 2 \int_0^{\sqrt{a^2-y^2}} \alpha(x,y)dx = \frac{1}{2}\ln\left(\frac{P_o}{P}\right) \tag{A1}$$

The factor of 2 after the first equality comes about because of the assumed even nature of the integrand. The factor of $\frac{1}{2}$ in the second equation arises because α is a *field* attenuation coefficient and the transmitted microwave power, P, is proportional to the square of the field strength. The phase shift of the scene beam also is an integrated quantity and may be treated in the same way.

We usually are interested in the *radial* dependence, not just the integrated value. Now, using $x^2 + y^2 = r^2$, we have

$$dx = \frac{rdr}{\sqrt{r^2 - y^2}} \tag{A2}$$

and

$$\bar{\alpha}L = 2 \int_y^a \frac{\alpha(r)rdr}{\sqrt{r^2 - y^2}} \equiv F(y) \tag{A3}$$

where F(y) is the measured chord integrated value of the attenuation.

The Abel transformation is

$$\alpha(r) = -\frac{1}{\pi} \int_r^a \frac{F'(y)dy}{(y^2 - r^2)^{1/2}} \tag{A4}$$

Thus, if F(y) is measured accurately enough to numerically evaluate F'(y) and the integral, $\alpha(r)$ may be computed. For the present problem, F(y) is measured on a fairly coarse chord spacing and the random error in F(y) is fairly large because of shot-to-shot variation. These conditions imply that a large error would be generated by numerically differentiating F(y) and numerically evaluating the integration. To get around these limitations, we invoke a least squares fit of the averaged data to an analytic function that

may itself be analytically Abel inverted. A particularly simple result occurs if we assume that F(y) is Gaussian:

$$F(y) = F(0) \, e^{-\frac{y^2}{2y_o^2}} \qquad (A5)$$

where we have determined F(0) and y_o from a least squares fit of the experimental data $F(y_i)$ to F(y). Now

$$F'(y) = -\frac{y}{y_o^2} F(0) \, e^{\frac{-y^2}{2y_o^2}} \qquad (A6)$$

Then

$$\alpha(r) = \frac{F(0)}{\pi y_o^2} \int_r^\infty \frac{y \, e^{\frac{-y^2}{2y_o^2}} \, dy}{(y^2 - r^2)^{1/2}} \qquad (A7)$$

Infinity is chosen as the upper bound here because the Gaussian is finite to $y \to \infty$. The integral is easily evaluated, and the result is

$$\alpha(r) = \frac{F(0)}{\sqrt{2\pi} \, y_o} \, e^{\frac{-r^2}{2y_o^2}} \qquad (A8)$$

Thus, the Abel inversion of a Gaussian of width y_o and peak F(0) also is a Gaussian of the same width and peak value of $\dfrac{F(0)}{y_o\sqrt{2\pi}}$, that is, the on-axis value of α is

$$\alpha(0) = \frac{F(0)}{\sqrt{2\pi} \, y_o} \qquad (A9)$$

We believe the choice of a Gaussian profile for the turbulent density channel is appropriate. The turbulent mixing is best described as a random process; Gaussian profiles thus are likely. The simple analytical fitting also makes this a convenient assumption.
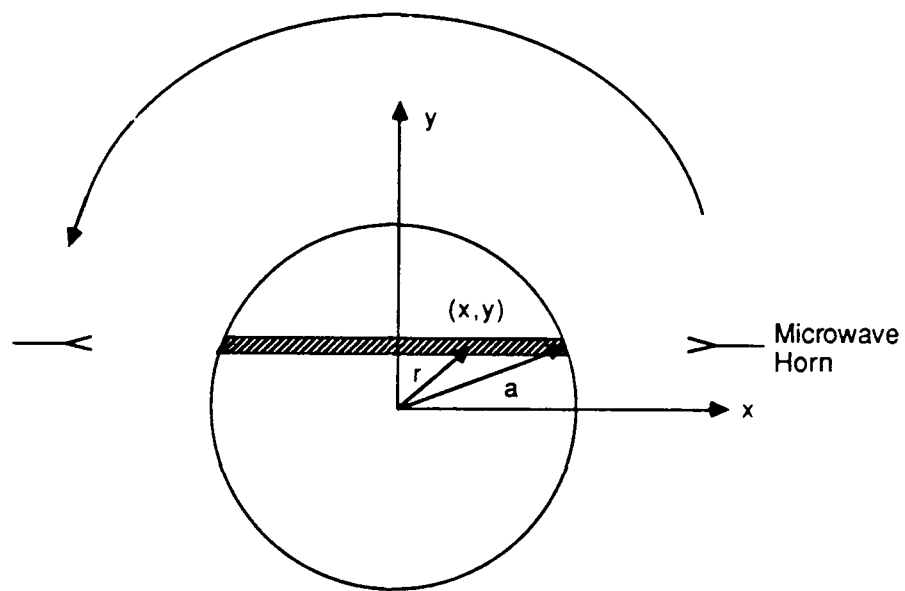
JA-8849-184

Figure A-1. Geometry for computing Abel inversion.

APPENDIX B

35-GHz ATTENUATION MEASUREMENTS

35-GHz ATTENUATION MEASUREMENTS

The 35-GHz attenuation measurements are included in this appendix to show the shot-to-shot variation and the unweighted least squares fit to Gaussian profiles and to illustrate the fact that many shots totally attenuated the 35-GHz microwaves. The error bars are determined by the standard deviation of the data. The number in parentheses beside each point is the number of shots used in the average. Error bars with upward pointing arrows indicate that at least one shot in a group was totally attenuated. The solid lines are the unweighted least-square fits to the Gaussian profiles. We only show those conditions where there was measurable attenuation. It is clear that for 0-kJ slow bank energy, the attenuation is very small, even at 2 ms, and is negligible for later times. The attenuation for 1-kJ shots is negligible after 4 ms. The attenuation for 2-kJ and 4-kJ shots was appreciable out to 6 ms.

The attenuation as a function of y was Abel inverted using the methods described in Appendix A; the resulting on-axis attenuation coefficients and Figures 6 and 8 were then used to determine equilibrium DC conductivities. The same techniques were used to reduce the phase shift data at the two frequencies to equilibrium DC conductivities. The DC conductivities obtained from attenuation coefficient data and phase shift data are shown in Figures 11 through 14.
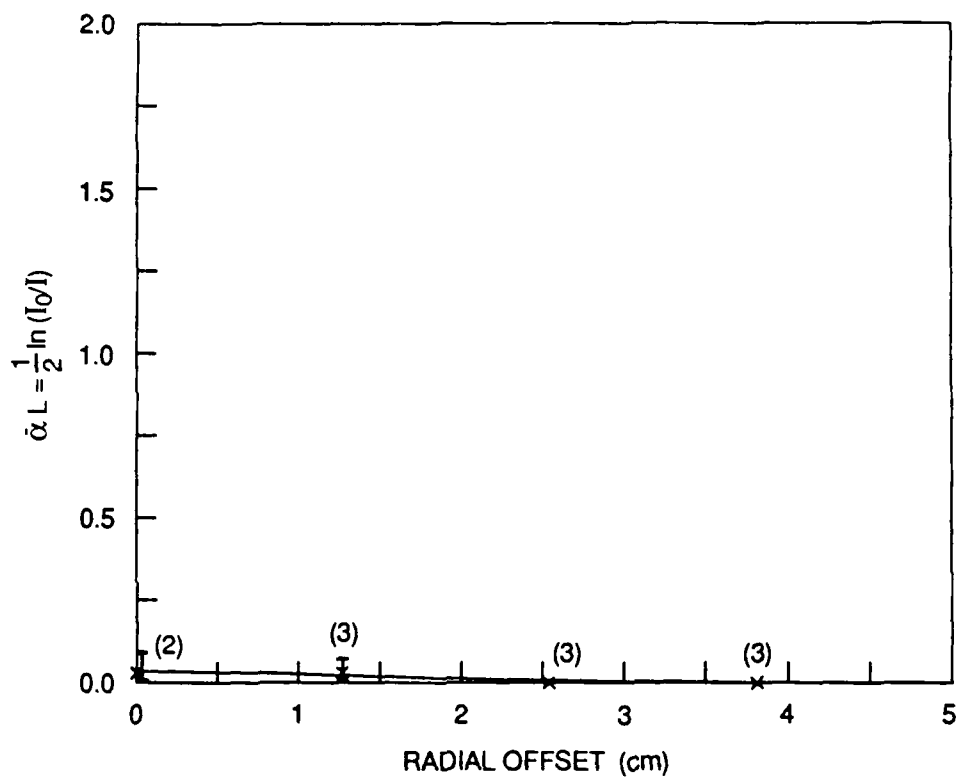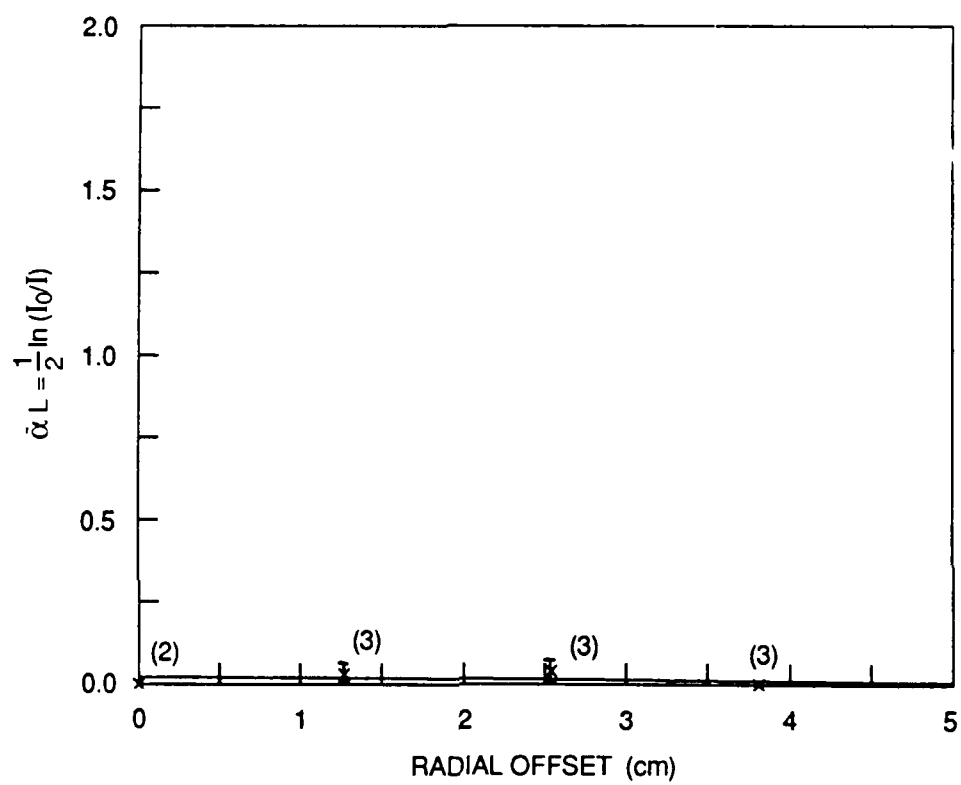
Figure B-1. 35 GHz chordwise absorption for 0 kJ slow bank energy at 2 ms.
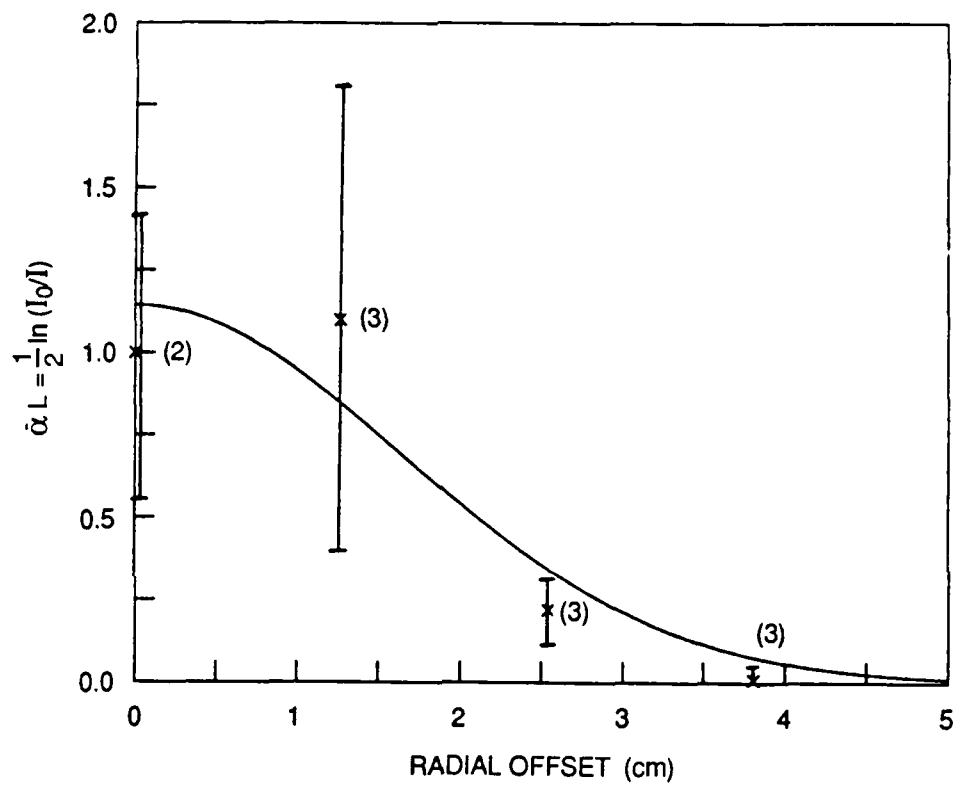
JA-8849-185
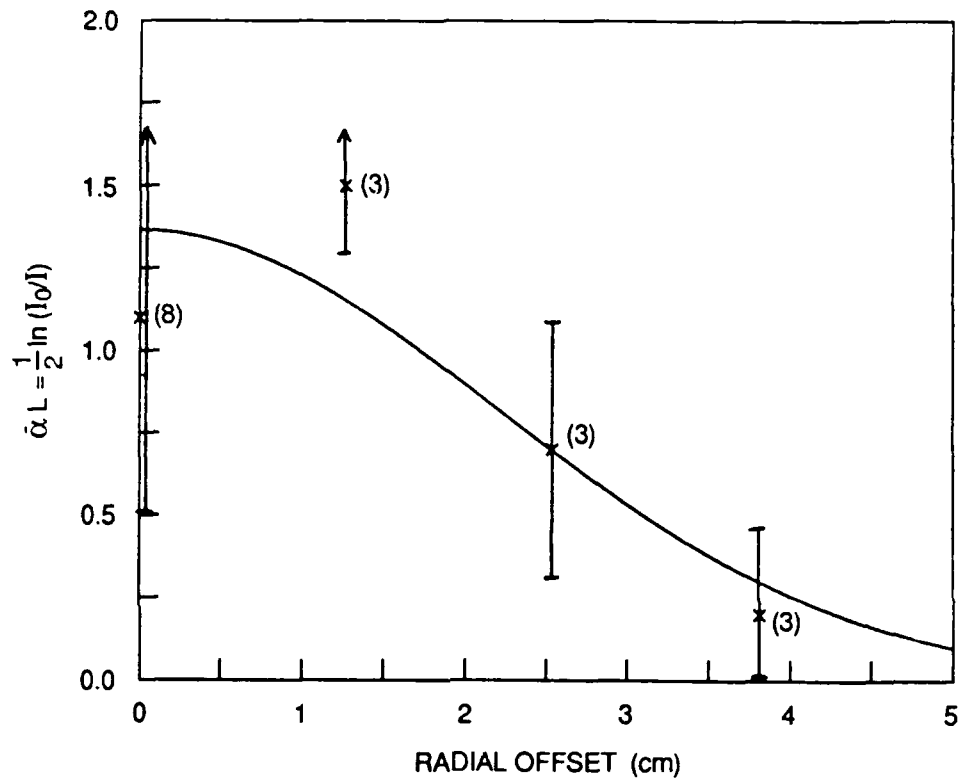
JA-8849-186

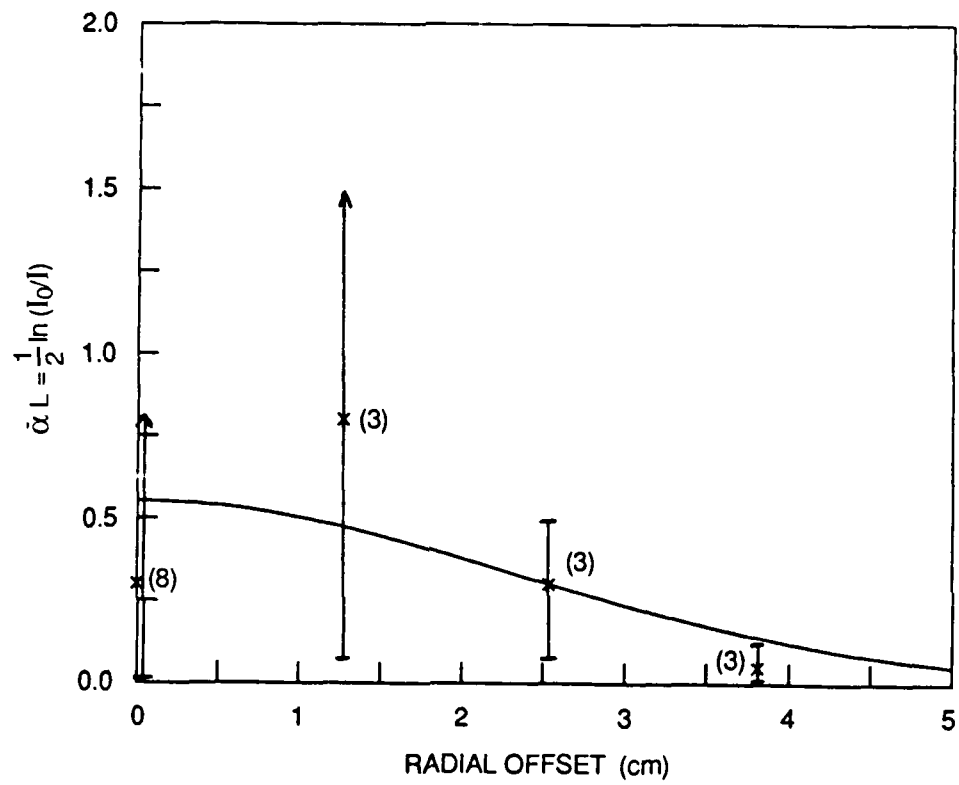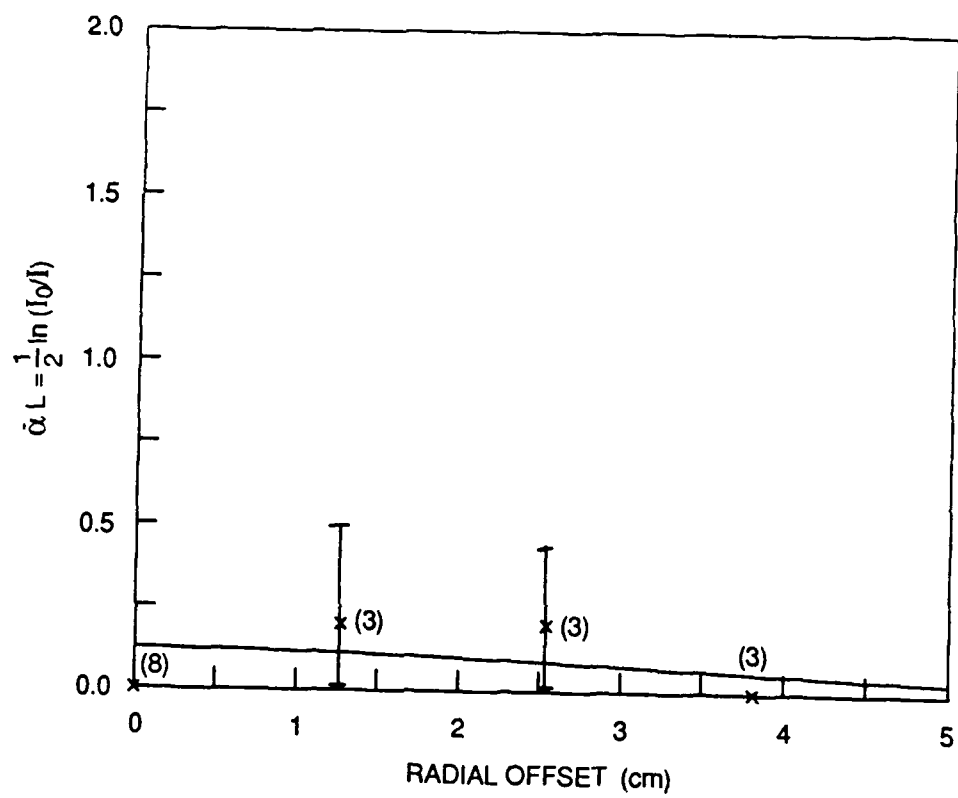Figure B-2. 35 GHz chordwise absorption for 1 kJ slow bank energy at 2 ms.

The y-axis is labeled $\bar{\alpha} L = \frac{1}{2} \ln (I_0/I)$ with values 0.0, 0.5, 1.0, 1.5, 2.0.

The x-axis is labeled RADIAL OFFSET (cm) with values 0, 1, 2, 3, 4, 5.

Data points are labeled (2), (3), (3), (3).

JA-8849-187

Figure B-3.   35 GHz chordwise absorption for 1 kJ slow bank energy at 4 ms.

Figure B-4. 35 GHz chordwise absorption for 2 kJ slow bank energy at 2 ms.

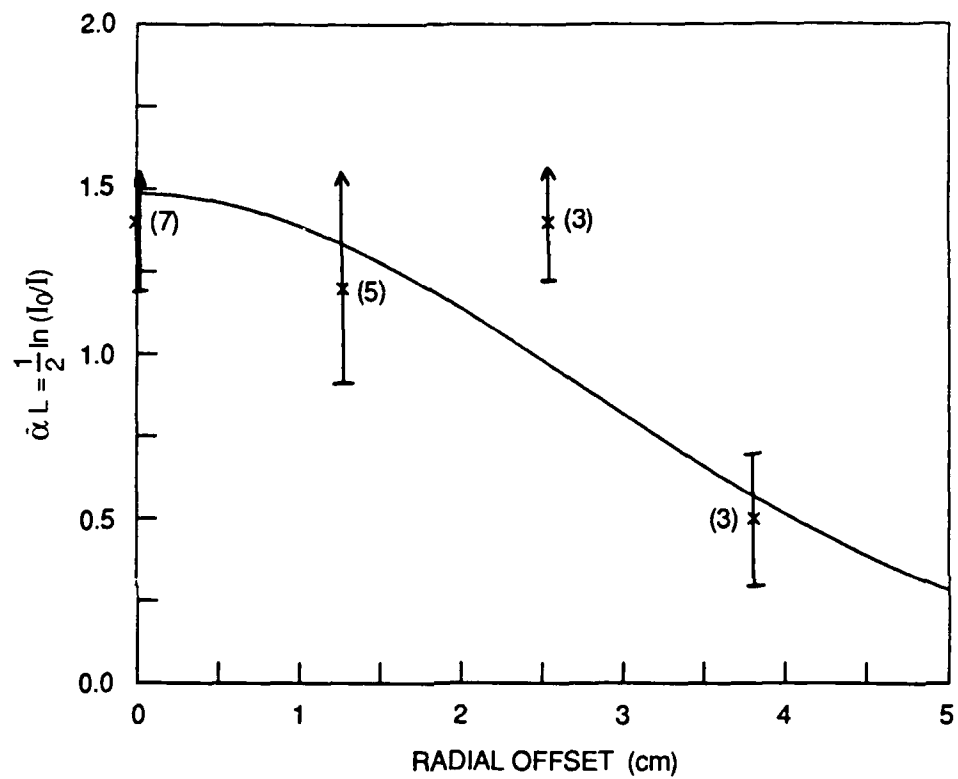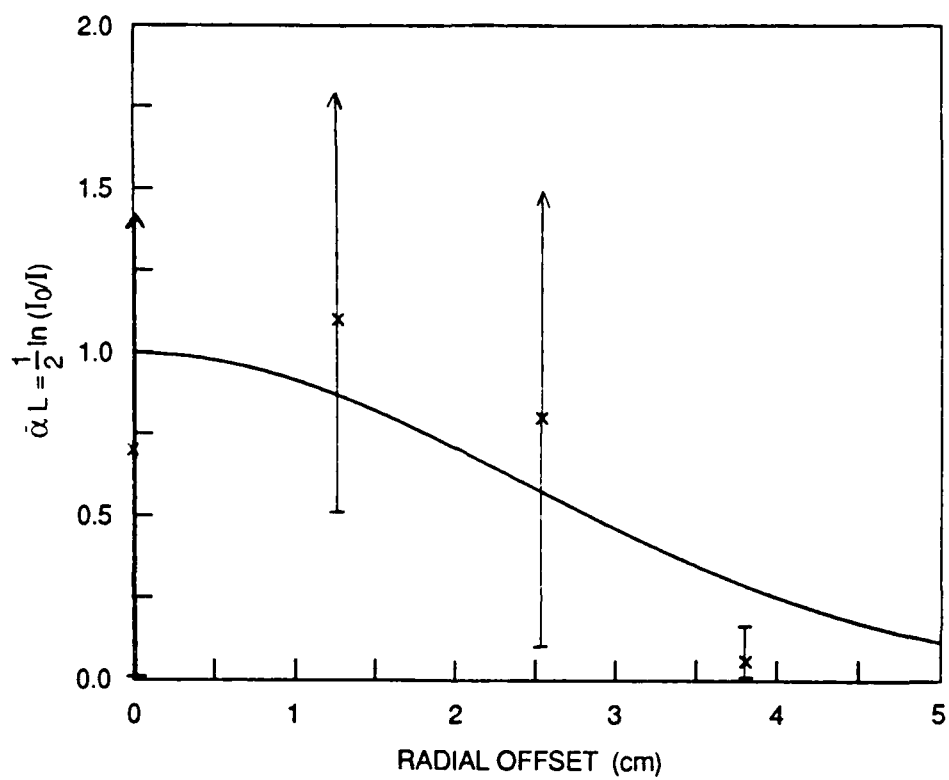Figure B-5. 35 GHz chordwise absorption for 2 kJ slow bank energy at 4 ms.

JA-8849-189

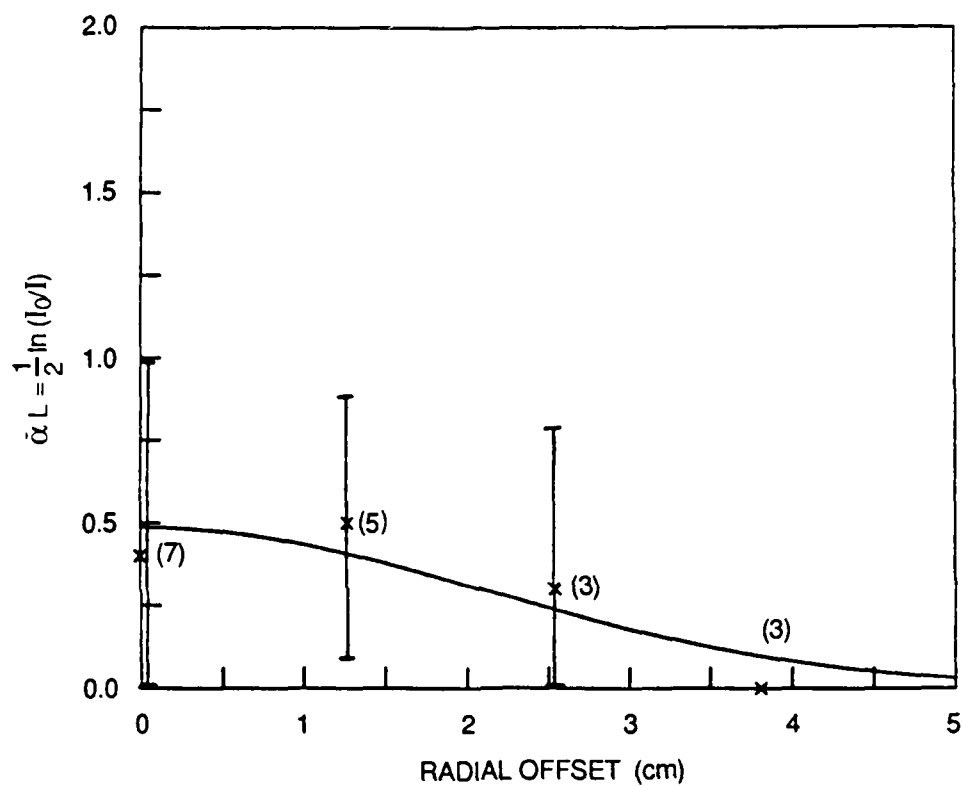Figure B-6.   35 GHz chordwise absorption for 2 kJ slow bank energy at 6 ms.

JA-8849-190

Figure B-7. 35 GHz chordwise absorption for 4 kJ slow bank energy at 2 ms.

JA-8849-191

JA-8849-192

Figure B-8.   35 GHz chordwise absorption for 4 kJ slow bank energy at 4 ms.

Figure B-9. 35 GHz chordwise absorption for 4 kJ slow bank energy at 6 ms.

JA-8849-193